Computer Methods in Applied Mechanics and Engineering 434 (2025) 117503

Contents lists available at ScienceDirect

Computer Methods in Applied Mechanics and Engineering

journal homepage: www.elsevier.com/locate/cma

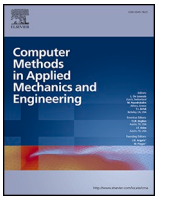

Integration of additive manufacturing process-induced material characteristics into topology optimization

Yeming Xian [a,*], Glaucio H. Paulino [b,c], David W. Rosen [a,d]

[a] George W. Woodruff School of Mechanical Engineering, Georgia Institute of Technology, Atlanta, GA 30332, USA
[b] Department of Civil and Environmental Engineering, Princeton University, Princeton, NJ 08544, USA
[c] Princeton Materials Institute (PMI), Princeton University, Princeton, NJ 08544, USA
[d] Institute for High Performance Computing, Agency for Science, Technology, and Research (A*STAR), Singapore

ARTICLE INFO

Keywords:
Topology optimization
Material anisotropy
Heterogeneous material
Additive manufacturing

ABSTRACT

Motivated by the mismatch between the mechanical performance calculated numerically in topologically optimized designs and that observed in the associated parts fabricated by additive manufacturing (AM) processes, we integrate material characteristics produced via AM processes into topology optimization at low computational cost, by introducing a density-based topology optimization formulation that designs coated structures composed of anisotropic materials. Literature reveals that microstructures and the resulting elastic properties of AM-fabricated parts are affected by local characteristics such as scan pattern and local part shape, which results in material anisotropy and heterogeneity. To account for properties of as-built additively manufactured parts, our formulation for design of coated structures produces anisotropic structures and accounts for heterogeneous material properties in local regions such as near the surface. The formulation takes the form of a multi-material volume-constrained compliance minimization problem and adopts a material interpolation scheme that accommodates material anisotropy and extracts the solid-void interface to enforce the coating. We present a range of examples in 2D and 3D to demonstrate the key ideas, in which a more general volume constraint setting is defined that allows the coated structure design method to accommodate multiple local or partial volume constraints, so as to facilitate flexibility of the volume constraint definition. Lastly, we prove by experimental validation that the integration of AM specific material characteristics in topology optimization generates more optimal designs for fabrication by AM.

1. Introduction and motivation

The design freedom offered by additive manufacturing (AM) has eased the fabrication of complex geometries such as those obtained using topology optimization; however, actual AM-fabricated parts may not exhibit the optimal mechanical performance expected from topology optimization that uses idealized isotropic properties. This is because these idealized properties are often altered during the AM processes, which made the topologically optimized design no longer optimal. During metal processes, properties of the raw material change after consolidation and cooling in a manner that is controlled by the local thermal history, leading to directional microstructure (hence anisotropy) as well as distinct phase transformation at local regions such as near surfaces. In polymer processes,

* Corresponding author.
E-mail addresses: paulaxian@gatech.edu, paulaxym@gmail.com (Y. Xian).

https://doi.org/10.1016/j.cma.2024.117503
Received 22 May 2024; Received in revised form 25 September 2024; Accepted 21 October 2024
Available online 30 November 2024

behavior of the printed material can change drastically from that of the bulk feedstock filament, for mechanical properties are highly dependent upon process parameters such as raster orientation and build direction, leading to potential material anisotropy within the build plane and along the build direction, as well as unique behavior at the outer shell of the part. This study is motivated by the need to improve the correlation between mechanical properties used in topology optimization and those observed in the associated AM parts. Our approach is to integrate material distributions that resemble those exhibited by parts fabricated using AM into the mechanics model underlying topology optimization, such that the material properties input to the numerical model are consistent with properties of the fabricated material. We put forward the following hypothesis: parts resulting from such an optimization method will have improved as-built mechanical performance compared to results using, for example, idealized isotropic mechanical properties.

To investigate how mechanical properties are altered during AM processes, we surveyed the literature on both metal and polymer-based AM processes, as both are relevant to our work. In literature related to polymer-based AM such as material extrusion (also known as fused filament fabrication (FFF)) [4-11], specimens were found to exhibit material anisotropy within the build plane depending on the infill pattern chosen. Furthermore, the skin/core approach used for depositing layers in FFF [11] suggested different material properties in the part contour region (or the perimeter) from the infill region. On metal-based AM processes such as laser and electron beam powder bed fusion, previous literature [21-28] reveals an inherent anisotropy of properties from observing the formation of grain structure and texture. Furthermore, the combined effects of several factors, such as scan patterns and local part shapes, result in different thermal histories at different locations of the part, which further leads to different microstructures between the regions near the surface produced by contour beam pass, and the inner regions where infill hatching occurs. Literature surveyed in both polymer-based and metal-based AM processes suggest a way to integrate AM process-induced material characteristics into design in an indirect and inexpensive manner: To model a structure using a topology optimization approach that sets apart the contour regions (i.e., the perimeter or near surfaces), and assigns to these contour regions a different mechanical behavior than the inner regions in the iteration process, such that each material only favors one region (either the contour regions or the inner regions) in the optimized structure. We recognize that other heterogeneous material properties may be present in AM fabricated parts; however, our focus is on modeling differences in near surface vs. inner regions that are often the most important heterogeneous properties.

To this end, a multi-material, volume-constrained, compliance minimization problem is considered for design of coated structures composed of anisotropic materials. A coated structure of this design method is composed of a bulk region and a coating region. The bulk region can be thought of as a base structure, while the coating region is a solid shell with a uniform thickness that envelops the bulk region. Separate (isotropic or anisotropic) material properties are assigned to material in the coating region (i.e., the coating material) and the bulk region (i.e., the bulk material). Both materials are assumed to be linear elastic. We adopt an approach from [1,2] that designs coated structures via an extension of SIMP (Solid Isotropic Material with Penalization, [3,44]), but modify the material interpolation scheme to accommodate anisotropic materials. With respect to the AM processes, the coating region of this design method corresponds to the outer perimeter produced during material extrusion or the near-surface regions created by contour beam passes in metal AM. These regions have distinct grain structures and textures compared to the interior of the part. Meanwhile, the bulk region represents the interior, where infill patterns are applied during both material extrusion and metal AM processes. We will explain more thoroughly in Section 3.3 how the coated structure design approach connects to the actual AM processes and serves the purpose of integrating AM process specific mechanical properties in topology optimization.

The main contribution of this work lies in integrating more realistic material properties, including anisotropy and heterogeneity at local regions, into a topology optimization framework, thereby better representing the material characteristics of as-built AM parts. From a numerical perspective, this work introduces the ability to incorporate two arbitrary materials—whether isotropic or anisotropic—as the coating material and the bulk material, respectively, within the optimization process.

The remainder of the paper is organized as follows: In Section 2, related work is reviewed, in which Section 2.4 addresses the research gap that is targeted in this work. In Section 3, the problem setting and formulation are provided, the material interpolation scheme that accommodates material anisotropy is discussed, the link between the numerical model and the AM processes is explored more thoroughly, and the sensitivities are derived. In Section 4, five numerical examples are provided and discussed to demonstrate the capabilities and potential shortcomings of the proposed approach. Section 5 includes a validation of our hypothesis via mechanical testing. Finally, in Section 6, conclusions are provided.

2. Literature review

This section presents literature survey on four topics related to our work: metal AM metallurgy & material characterization, polymer-based AM mechanical properties characterization, incorporating material anisotropy in multi-material topology optimization, and incorporating AM process-induced mechanical properties in topology optimization. For the first topic, we focus on metal parts that result from powder bed fusion (PBF) processes. Previous works on metal-based AM processes give broad and comprehensive insights, both on microscopic and macroscopic levels, on the material characteristics of metal AM-fabricated parts. The second topic focuses on material extrusion (or FFF). In the third and fourth topics, we explain, respectively, the research gap with respect to integrating material anisotropy and integrating the effect of AM process on mechanical properties in topology optimization that this work intends to contribute to.

2.1. Metallurgy and mechanical properties characterization on metal AM

A lot of research groups have studied the grain structure and texture of simple geometries fabricated using metal AM processes such as selective laser melting (SLM) and electron beam melting (EBM). We discuss a few representative works below. Murr and his co-

workers [21] conducted a comprehensive review on characterizing and visualizing the microstructures of several types of metal or alloy components produced by the PBF processes. One of the characteristics they had in common was directional microstructure during solidification. Al-Bermani et al. [23] fabricated fully dense Ti-6Al-4V cylindrical samples by EBM and observed that columnar grains make up the bulk microstructure during solidification, a finding which coincided with that of [21]. The columnar nature of the grains indicates an inherent anisotropy of properties. At the cooling stage, these grains transform to different microstructures depending on the cooling rate and the local temperature, a finding which agreed with that of [22], another study by Murr et al. on Ti-6Al-4V open cellular foams, which showed that microstructure and material properties are highly dependent on the local temperature history during the EBM process. Antonysamy et al. [24] investigated the effect of local geometry on the grain structure in Ti-6Al-4V components produced by EBM. Observations were consistent between samples of different types of build geometry: Distinct differences were found between the grain structure and texture produced by the contour beam pass and in-fill hatching of the EBM build cycle. These differences in microstructure, which cause differences in mechanical properties, can be captured numerically in the coated structure method introduced in [1]. Specifically, the effects of contour passes can be modeled by coating material and the effects of in-fill hatching correspond to bulk material. We will provide more detail on this work and how it served our formulation in Section 3.3.

Other than studying on the microscopic level, quite a few publications carried out mechanical testing and measured properties of various types of metal printed alloys. Differences in mechanical properties influenced by building orientations were investigated. In [25], four metallic alloys were fabricated using PBF processes. Bending and tensile tests showed that some material properties showed larger differences between vertically and horizontally built specimens than others. Similar study was done on an aluminum-silicon alloy in [26], in which stress-strain curves of specimens built in two orientations showed a significant difference in strengthening behavior and elongation at fracture. Results in both publications showed anisotropy in SLM produced material. Austenitic stainless steel specimens were built via SLM at different build angles in [27]. Testing results showed very different tensile strength between horizontal and vertical specimens, and demonstrated a much larger anisotropy than its wrought counterpart. This orientation dependence of the tensile properties was explained from a crystallographic point of view in [28].

2.2. Effect of process parameters on mechanical properties in polymer-based AM

Numerous literature on FFF demonstrated via experimental testing how printing parameters such as build orientation, layer thickness, infill density and pattern, and number of shell perimeters, among others, have a substantial effect on the quality and mechanical properties of FFF printed parts. Riddick et al. [5] investigated the effects of build direction and raster orientation (or raster angle) on the mechanical response of FFF parts, by conducting tensile tests until failure on ABS (Acrylonitrile-Butadiene-Styrene) specimens. The tensile strength and modulus, and elongation-at-break were found to be highly dependent upon the raster orientation and build direction, which implied anisotropy in mechanical response. Uddin et al. [10] conducted tensile and compressive tests of ABS specimens and had different observations from Riddick et al. [5] regarding the effects of the parameters. Casavola et al. [6] included a similar study on raster orientation using single layer ABS and PLA (polylactic acid) specimens. Es-Said et al. [7] carried out a thorough study on the effect of raster orientation using ABS specimens via tensile and three-point bend tests. Their testing results matched those of Riddick et al. [5] to some extent, and indicated that mechanical properties within the build plane may be anisotropic depending on the raster orientation chosen.

In the examination of the effects of parameters on PLA specimens by Akande et al. [11], difference in flexural modulus between 20% and 100% infill densities was found to be more noteworthy when a higher layer thickness was used, showing interdependence between process parameters. Although not investigated further, the authors highlighted the importance of cross section perimeters by explaining the “skin/core” approach in FFF, in which the “skin” refers to the perimeter, and “core” the infill region in each layer. Torres et al. [9] used Taguchi method to investigate the influences of a series of parameters, including build direction, infill density, as well as the existence of perimeter region, on the mechanical properties of PLA specimens. Results revealed that the fully dense perimeter tool paths add strength to the structure. The authors stressed the influence of the perimeter tool path on mechanical properties. In line with the coated structure method [1], the perimeter tool paths correspond to the coating, while the in-fill corresponds to the bulk region. In an FFF part, the perimeters and in-fills have significantly different mechanical properties, which can be modeled by a coated structure. ANOVA F-values were used to rank the influence level of each parameter on each mechanical property. Ranking results showed that infill density is the most influential parameter; perimeter ranked at the fourth most influential processing parameter overall, closely following layer thickness and extrusion temperature. Similar to [9], Lanzotti et al. [8] studied the combined effect of several parameters on the mechanical properties, and showed that interactions between the parameters were significant.

2.3. Integration of material anisotropy in multi-material topology optimization

Exploring material anisotropy in topology optimization dates back to 1988 [12], in which Bendsøe and Kikuchi investigated material distribution problems by introducing periodically distributed microscale voids in a homogeneous and isotropic substance material. The homogenized macroscopic material exhibits anisotropic behavior. In that paper and in several papers that followed [3,29,30], the layout problem was defined as a function of the microstructure’s porosity and orientation, such that pointwise material orientation was optimized as well. Authors used the finding that orientation of a microscale void could be identified as the principal strain or stress direction at that location in the case of an orthotropic material, to achieve extreme strain energy density. Stegmann and Lund [31] proposed a novel design method, Discrete Material Optimization (DMO), that optimizes orientation of anisotropic material (such as directions of the fibers in composite laminates) in a discrete manner: instead of treating material orientation as a continuous design variable as in [12], the DMO discretizes the orientation field into a set of candidate orientations, or we can also say, candidate

materials, then the optimal orientation/material of an element is chosen via an interpolation scheme that penalizes material mixing and pushes element densities towards 0 and 1. The DMO laid a natural foundation for multi-material optimization, for its material interpolation scheme is well equipped to handle an arbitrary number of materials. Ref. [15] was also about concurrent design of density and orientation of anisotropic material. Compared to the homogenization design approach [12] in which rotation angle was the design variable, this work used Cartesian components of the material orientation vector as design variables as a relaxation of the design space, with the aim of solving the difficulties that angular design variables presented. Angular representation may cause the solution to fall into local minimum and become non unique (problem of 2pi ambiguity).

Compared to single-material optimization, multi-material topology optimization enlarges the design space because it introduces more variables and options for the distribution and selection of materials, allowing for a broader exploration of potential design configurations that can better meet the optimization objectives [46]. The Solid Isotropic Material with Penalization (SIMP) method was first extended in [47-49] to accommodate three material phases - two materials in the form of continuous microstructures and void - with extreme thermal expansion. The formulation introduces a topology design variable for material/void distribution and a second variable for material selection that interpolates between the two material phases. This generalized approach utilizes two sets of design variables – one to track the optimal topology and the other to control material allocation between the two phases at each material point. The SIMP and the RAMP (Rational Approximation of Material Properties) [50] schemes are further generalized in [51,52] to an arbitrary number of materials. Their proposed interpolation schemes prevent material mixing and enforce the sum of material densities to be less than or equal to one via linear constraints. Yin and Ananthasuresh [53] proposed a multi-material interpolation scheme using Gaussian peak functions that allows the number of design variables to remain constant as the number of candidate materials grows. An alternating active-phase (AAP) algorithm was proposed in [54] that breaks down the multi-material optimization problem into a sequence of two-phase sub-problems. Implementing the AAP algorithm involves introducing an external loop that iterates over a standard two-phase topology optimization framework that can be solved using conventional binary phase optimization techniques, such as the OC method. This approach ensures that the total material density at any point does not exceed one. The geometry projection method developed by [55] for designing multi-material lattices composed of cylindrical struts introduces a no-cut constraint, resulting in designs that are more suitable for manufacturing by producing only complete struts. Anisotropic candidate materials were considered in [56], which introduced a method for optimally distributing anisotropic candidate materials in the topology optimization design domain using self-assembled structures, specifically through diblock copolymers. Huang and Li [57] designed multi-material structures using a linear material model incorporated with a floating projection constraint, and proposed guidelines for selecting candidate materials from the database. The linear material interpolation scheme can be extended to anisotropic materials [57].

In the context of truss topology optimization, a multi-material approach to the minimum compliance problem was introduced in [58], employing a design update method called ZPR that independently updates design variables for each volume constraint. This ZPR method was later improved in [59] to account for both positive and negative sensitivities, while also integrating material nonlinearity through a novel material interpolation scheme. Ref [60,61] introduced the Color Level Set method, which extends the level sets approach to multiple materials. This method uses multiple level-set functions to represent various materials, similar to how primary colors combine to form different shades. Phase-field methods have also been applied to multi-material topology optimization [62-65]. For instance, a generalization for any number of phases was proposed in [63] using a modified Cahn–Hilliard equation, and in [64] using a modified Allen–Cahn equation. Evolutionary optimization methods have also been applied for multi-material topology optimization [66].

2.4. Integration of AM process induced mechanical properties in topology optimization

As we have seen in Section 2.3, many topology optimization methods have considered material anisotropy. However, not as many have incorporated AM process specific material anisotropy. Within the limit of linear elasticity, previous work in the literature has mainly focused on optimizing the AM build orientation, because mechanical properties have a more obvious change in the printing direction in many AM processes. For example, Ulu et al. [13] introduced a surrogate-based optimization approach which determines the optimal build direction of a polymer-based process that maximizes the safety factor against yielding along all principal directions. According to Liu et al. [14], this topic of finding the optimal build orientation can be readily solved using methods such as continuous orientation design [15] which was reviewed in Section 2.3. Liu et al. [14] also discussed multi-build direction AM which prints a part in multiple directions. Although multi-direction optimization can be readily solved using multi-material topology optimization methods, to manufacture a design produced using multi-direction optimization requires an AM process with consistent manufacturing freedoms [16], such as directed energy deposition technology with five degrees of freedom [43]. Our work on coated structure matches with the much more common AM approach that is limited to horizontal planar layers (single direction of fabrication).

Other than incorporating build orientation in topology optimization, there is more to consider regarding the effect of AM process on mechanical properties. It is known that AM processes produce anisotropy, in fact, FFF printed parts are known to have orthotropic properties [6,9]. Many researchers have used properties that were measured via experiments as material input in topology optimization. However, the experimentally measured elastic constants are global properties averaged over the test specimen, whereas mechanical properties are affected by quite a few local characteristics such as scan patterns, local part shapes, and temperature history [17], which indicates a need to investigate AM-induced material characteristics on a microstructure level. For one, we have seen in Sections 2.1 and 2.2 that in both metal and polymer AM-printed parts, there exist local regions such as near-surface where microstructures and the resulting elastic properties vary from the experimentally measured global properties. Dapogny et al. [18] considered this material heterogeneity in FFF and used the level set method to design shell-infill structures given a scanning strategy. This study integrated the tool path in topology optimization. Groen et al. [19] used a homogenization method to design coated structures with

orthotropic infill material, such that the design space is relaxed to allow for periodic composite microstructures as infill. Wadbro and Niu (2019) [45] also introduced a multi-scale topology optimization framework for coated structures with anisotropic infills made of periodic microstructures. A Porous Anisotropic Material with Penalization (PAMP) method was utilized to concurrently optimize the topology at the macro- and micro-scales. The homogenized material properties of the periodic lattice infill may be anisotropic. Our work will also demonstrate that the consideration of anisotropic infills is beneficial for the mechanical performance of AM fabricated parts [20].

Our work specifically addresses the research gap related to the anisotropy difference between near-surface and inner regions. As a result, other important AM parameters, such as building orientations, cooling rates, and layer thickness mentioned in Sections 2.1 and 2.2, are not considered in this study. It is important to note that investigating the influence of these additional parameters is a valuable area and requires further research.

3. Formulation

This section first presents the problem formulation that we use for the design of coated structure considering material anisotropy. Next, we discuss the material interpolation scheme used to incorporate material anisotropy and to obtain the effective material properties of intermediate element densities. We then explain how this design method is linked to the actual AM printing procedure and facilitates fabrication. Finally, we introduce the density filter used in this method briefly, before presenting the sensitivity analysis of the objective function.

3.1. Problem formulation

$$\begin{aligned} &\min_{z_1,\dots,z_n} f = \boldsymbol{F}^T \boldsymbol{U}(\boldsymbol{z}) \\ &\textit{subjected to}: \quad g = \frac{\sum_{l=1}^{n} A_l m_V(y_l)}{\sum_{l=1}^{n} A_l} - \bar{v} \leq 0 \\ &\text{with}: \quad \boldsymbol{K}(\boldsymbol{z})\boldsymbol{U}(\boldsymbol{z}) = \boldsymbol{F} \end{aligned} \tag{1}$$

The formulation in Eq. (1) is stated as a multi-material problem for volume constrained compliance minimization, that accommodates two candidate materials (one for bulk region, the other coating region) and a global volume constraint associated with both materials. The objective function f is the compliance of the structure, function g is the volume constraint. The design vector is formed as $\boldsymbol{z} = [z_1, .., z_n]^T$, n is the number of elements. A_l is the area or volume of element l, $\bar{v}$ is the prescribed volume fraction limit. m_V represents a volume interpolation function of the smoothed density y_l of element l. The formulation is governed by a state equation, approximated

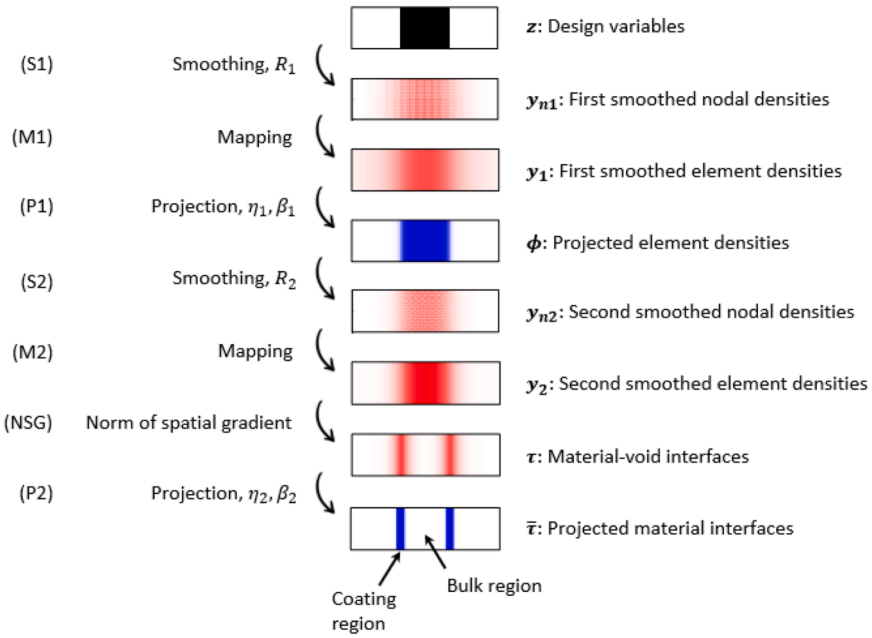

Fig. 1. Material interpolation process for extracting the material interfaces (i.e. for separating the coating region and the bulk region). The notation and description of each variable in the process is provided on the right, while the process/operation applied to the variables at each step is given on the left (figure adapted from [1]).

by the finite element method, in which $\boldsymbol{K}$, $\boldsymbol{U}$, and $\boldsymbol{F}$ are the stiffness matrix, displacement field, and force vector respectively. Although not shown in Eq. (1), another interpolation function for the stiffness is needed to solve $\boldsymbol{U}$, it relates the density function to the stiffness at a point [33].

Because both negative and positive values appear in the sensitivity analysis of the objective function, we adopt the MMA (method of moving asymptotes) update scheme [32]. The implementation is built on top of `PolyTop` [33], a single-material topology optimization framework on unstructured polygonal meshes using a modular structure that separates the optimization from analysis routines [35].

3.2. Material interpolation

Fig. 1 shows the process of identifying the material-void interfaces, which is explained in [1] in detail. This process separates the material-void interfaces from the base structure to construct the coating region. The design variables $\boldsymbol{z}$ are firstly subject to two rounds of smoothing (or filtering) operations using a PDE-based filter which will be briefly explained in Section 3.4. Then the material-void interfaces (named "coating region" in Fig. 1) are obtained via spatial gradients of the second smoothed density field $\boldsymbol{y}_2$. In Fig. 1, the steps that are plotted in red result from a smoothing operation, while the steps plotted in blue indicate projected fields in which density values are pushed toward 0 or 1. The thickness of the coating region is a function of the two filter radii, R_1 and R_2. Coating thickness increases when R_2 increases and/or when R_1 decreases. Since the second smoothing operation is directly related to the derivation of material interfaces, the coating thickness is more sensitive to the value of R_2 than to R_1. In [1], materials are assumed to be isotropic, the coating region is assigned a solid material, while the bulk region is assigned a less dense and less stiff material. The volume and stiffness interpolation functions of an element l for isotropic materials are shown in Eq. (2) and Eq. (3) respectively; V_l in Eq. (2) corresponds to the volume interpolation $m_V(\boldsymbol{y}_l)$ used in Eq. (1).

$$V_l = \overline{\tau}_l + \lambda_m \phi_l (1 - \overline{\tau}_l) \tag{2}$$

$$E_l = \varepsilon E_0 + (1-\varepsilon)\overline{\tau}_l^p E_0 + (1-\varepsilon)\lambda_E \phi_l^p \left(1 - \overline{\tau}_l^p\right) E_0 \tag{3}$$

where E_0 is the Young's modulus of the solid coating material, ε defines the ersatz material that is used to avoid singularities in the stiffness matrix. ϕ_l is an intermediate density value of element l, $\overline{\tau}_l$ is an element density that highlights the material-void interfaces. The two density fields ϕ and $\overline{\boldsymbol{\tau}}$ are both obtained through a projection function [38] during steps (P1) and (P2) as indicated in Fig. 1. Power p is the SIMP [3] penalty parameter. Three parameters are increased gradually via a continuation scheme in this work: the power p, and the projection parameters β_1 and β_2 used during steps (P1) and (P2) as indicated in Fig. 1.

Two scale factors, λ_m and λ_E, are used to define the relative mass density and the relative stiffness, respectively, of the bulk material compared to the coating material. We can interpret the factor λ_m as either a coefficient of the interpolated volumes of the bulk material, or mass density of the bulk material. The interpolation functions make material mixing between the two regions (coating region and bulk region) uneconomical: If element l belongs to the coating region, then its $\overline{\tau}$ value approaches 1, and $V_l \approx 1,\ E_l \approx E_0$. If it belongs to the bulk region, then its $\overline{\tau}$ value approaches 0, and $V_l \approx \lambda_m \phi_l \approx \lambda_m,\ E_l \approx \lambda_E E_0 \phi_l^p \approx \lambda_E E_0$. The volume interpolation functions of the two materials are separated in Eq. (2): the term $\overline{\tau}_l$ represents the interpolated volume of the coating material, while the term $\lambda_m \phi_l (1 - \overline{\tau}_l)$ represents that of the bulk material. Similarly, the terms $(1-\varepsilon)\overline{\tau}_l^p E_0$ and $(1-\varepsilon)\lambda_E \phi_l^p \left(1 - \overline{\tau}_l^p\right) E_0$ in Eq. (3) represent the interpolated stiffnesses of the coating and the bulk materials respectively. As we will see next in Eq. (4), separating the interpolation functions of the two materials is essential to building the material interpolation scheme when material anisotropy exists.

In the isotropic case, it is sufficient to interpolate a scalar Young's modulus and compute a single constant stiffness matrix. An anisotropic material, however, is characterized, not by the Young's modulus alone, but by the elasticity matrix D that constitutes the element stiffness matrix. Thus, it is necessary to interpolate the element stiffness matrix $\boldsymbol{k}_l$ for each element l as shown in Eq. (4). Volume interpolation is the same as in Eq. (2) of the isotropic case.

$$\begin{aligned} \boldsymbol{k}_l &= w_{l1}\boldsymbol{k}_{l1}^0 + w_{l2}\boldsymbol{k}_{l2}^0 \\ w_{l1} &= \varepsilon + (1-\varepsilon)\overline{\tau}_l^p \\ w_{l2} &= \varepsilon + (1-\varepsilon)\phi_l^p \left(1 - \overline{\tau}_l^p\right) \end{aligned} \tag{4}$$

For any term in Eq. (4) that has two indices, the first index indicates the element, the second index indicates the material, where index 1 is the coating material and index 2 the bulk material. Hence, $\boldsymbol{k}_{l1}^0$ and $\boldsymbol{k}_{l2}^0$ are the element stiffness matrices of element l associated with the coating and the bulk materials respectively. The element stiffness matrix for each material in each element is constituted by the elasticity matrix: $\left(\boldsymbol{k}_{li}^0\right)_{jk} = \int_{\Omega_l} \boldsymbol{B}_j^T \boldsymbol{D}_i \boldsymbol{B}_k dxdy$, where $\boldsymbol{D}_i$ is the elasticity matrix of material i, $\boldsymbol{B}$ is the strain-displacement matrix of interpolation function derivatives. The terms ε, ϕ_l, $\overline{\tau}_l$, and p were defined in Eqs. (2) and (3). We can see that $\boldsymbol{k}_l$ is an interpolation between the element stiffness matrices of the two materials. The weights of the coating material and the bulk material are w_{l1} and w_{l2}, respectively, which are the penalized densities of element l associated with the two materials. Material mixing is penalized through the w terms: If element l belongs to the material interfaces (or coating region), then $\overline{\tau}_l$ approaches 1, which makes $w_{l1} \approx 1,\ w_{l2} \approx \varepsilon$. If it belongs to the interior (or bulk region), then $\overline{\tau}_l$ approaches 0, which makes $w_{l1} \approx \varepsilon,\ w_{l2} \approx \phi_l^p \approx 1$.

This material interpolation scheme including material anisotropy was inspired by [35,36], which were based on a Discrete Material Optimization (DMO) interpolation first introduced in [31]. It eliminates the scale factor λ_E (for defining the relative stiffness) in Eq. (3),

and allows us to input two arbitrary anisotropic (or isotropic) stiffness tensors as the coating and bulk properties.

3.3. Link to AM process

We will show in this sub-section that our optimization method connects with actual AM printing processes and facilitates manufacture. It will be revealed how the material interpolation scheme in Section 3.2 reflects the effects of AM process parameters on mechanical properties, both in metal and polymer AM-fabricated parts.

We have seen from literature review that in additively manufactured metal parts, local properties (in small features and along part boundaries) vary from bulk properties [24,23,22]. This is demonstrated by Fig. 2 [24]. It provides reconstructed β-grain structure first formed on solidification of an EBM-built Ti-6Al-4V sample, in which a 1.5 mm-thick vertical wall is built on top of a 5 mm-tall base. The fabricated sample is shown in Fig. 2(b). The grain structure in Fig. 2(a) corresponds to a section view in the $R_X - N_Z$ plane of the third thin wall sample from the right. The dotted line indicates the transition from the wide section (or thick base) to the thin wall. In the wide section of the sample (below the dotted line), columnar grains grow upward through many deposited layers, some extending across the thick-thin transition. This agrees with the observation of directional microstructure in [21]. In the thin wall section (above the dotted line), toward the center line where infill hatching occurs during printing, we observe the same columnar grains growing vertically as those in the thick base. By contrast, contour beam pass produced a complex skin layer with a different grain structure on the two sides of the wall. Fine inward-growing curved β-grains appear at the wall faces; further, long thin grains can be seen between the inward curved grains at the wall faces, and the regular vertical grains in the center. Further interesting features were identified within the skin layer according to [24], which revealed the skin (or the part boundary) itself consisted of several layers of different microstructures. This implies material heterogeneities in local geometry (e.g., near surfaces, in thin walls, and in section transition regions).

To simplify the numerical model in this work, we assume the heterogeneity within the part boundary itself is negligible, and only define two distinct material regions – captioned "bulk region" and "coating region" respectively in Fig. 2 – to demonstrate local heterogeneity of metal AM parts. This assumption allows us to use the coated structure model in [1]: the material regions produced by infill hatching and contour pass during metal printing can be modeled by the bulk and the coating regions, respectively, illustrated at the bottom of Fig. 1. Such is how our numerical method is well connected to the material characteristics illustrated in metal PBF parts.

Similar connection can be found in parts manufactured via material extrusion. Literature on the FFF process such as [8,9] revealed that properties of the shell perimeter vary from the infill region of the printed part, and that the influence of the perimeter region on mechanical properties should be explored. Fig. 3(a) shows the inside of a three-point bend PLA test specimen which was topologically optimized and then printed via FFF, showing a section cut along the build plane. Difference between the perimeter shell and the infill region is distinct: The infill region is made up of horizontal linear raster lines with a density of 25%, while the perimeter shell is made up of continuous roads of solid filament that trace the contour of the object. Another example of FFF is a single layer ABS specimen with a raster angle of 45°, Fig. 3(b) [6] shows it lying in the build plane. It is clear that two contour lines were deposited as the perimeter shell before the infill region was filled by inclined beads.

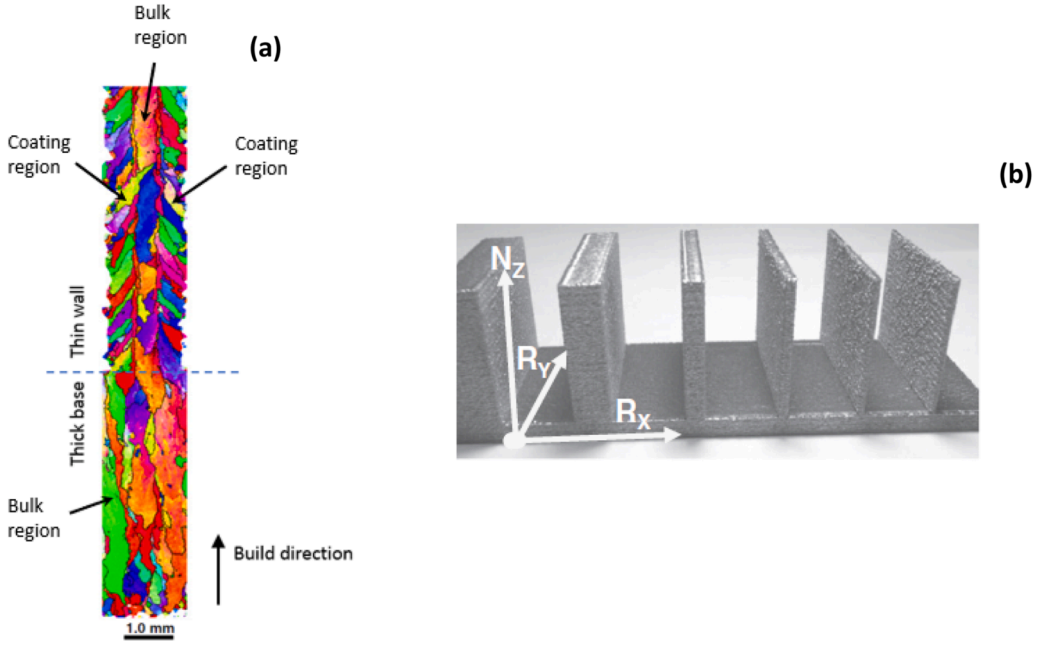

Fig. 2. (a) Reconstructed EBSD map on Rx-Nz cross sectional view of a thin wall specimen built on top of a thick base, showing grain structure of the specimen; (b) The corresponding specimen produced using EBM (figure adapted from [24]; color online).

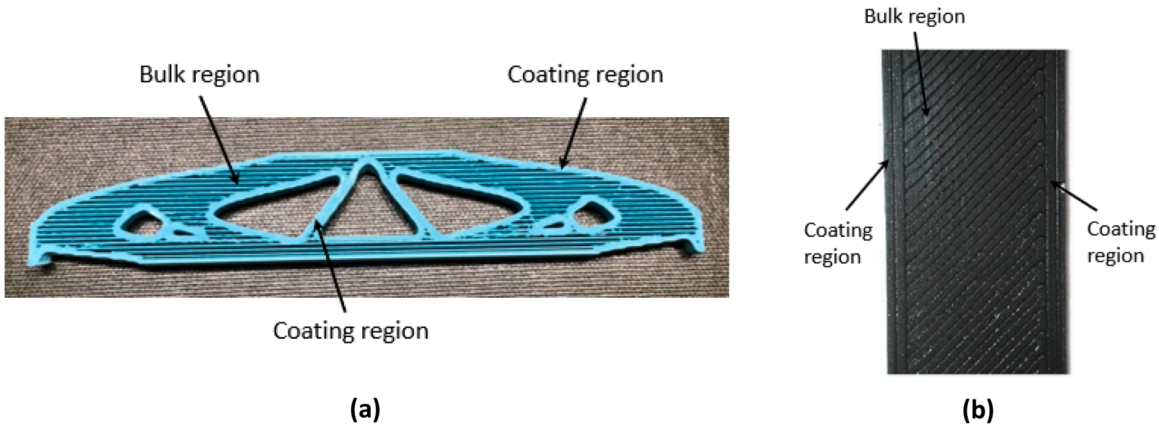

Fig. 3. (a) Section view showing the build plane of a topology optimization result printed via FFF process (color online); (b) A single layer ABS specimen with 45 raster angle (figure borrowed from [6]).

We have seen in Section 2.2 that the infill region and the perimeter of an FFF-printed part are controlled by different process parameters: Properties of the infill region are mainly affected by parameters such as raster orientation and infill density, while properties of the perimeter vary with the number of shell contours. This leads to the idea of defining two distinct material regions and separating their mechanical properties in the material interpolation scheme, to demonstrate local heterogeneity of polymer-based AM parts: the material regions produced by infill raster pattern and perimeter shell during material extrusion correspond to the bulk and the coating regions in the numerical model respectively. This connection of the numerical model with the material characteristics of FFF parts can be seen in Fig. 3, in which the captions "bulk region" and "coating region" correspond to the same captions as those in Fig. 1.

3.4. Density filter

The original coated structure method [1] uses a density filter based on the solution of a Helmholtz-type partial differential equation (PDE) as shown in Eq. (5), in which z_e is the design variable, y_e is the to-be-calculated filtered density of element e, and r is the filter radius. The filter function value decays in a nonlinear manner with increasing distance from the current element.

$$-r^2\nabla^2 y_e + y_e = z_e \tag{5}$$

As explained in [34], Eq. (5) is discretized via the method of weighted residuals and by using polynomial interpolation function as the weight function. After applying Green's first identity and assembling all the elements, a system of linear equations in the form of Eq. (6) is obtained where the unknowns become the nodal densities of the filtered field, $\boldsymbol{y_n}$. This corresponds to the smoothing steps $\boldsymbol{z}\rightarrow\boldsymbol{y}_{n1}$ and $\phi\rightarrow\boldsymbol{y}_{n2}$, denoted by (S1) and (S2), respectively, in Fig. 1. For more details on the derivation of matrices $\boldsymbol{K}_f$ and $\boldsymbol{T}_f$ in Eq. (6), please refer to [34].

$$\boldsymbol{K}_f\boldsymbol{y_n} = \boldsymbol{T}_f\boldsymbol{z} \tag{6}$$

As shown in Fig. 1, the smoothing step (S1) is followed by a mapping operation (M1) to obtain the filtered element density y_e from the nodal densities $\boldsymbol{y}_{n1}$. The smoothed density of element e is a weighted sum of the nodal densities constituting element e. The weight factor H_k of each node k depends on the interpolation function associated with this node, as shown in Eq. (7). The mapping step corresponds to the steps $\boldsymbol{y}_{n1}\rightarrow\boldsymbol{y}_1$ and $\boldsymbol{y}_{n2}\rightarrow\boldsymbol{y}_2$, denoted by (M1) and (M2), respectively, in Fig. 1.

$$\begin{aligned} H_k &= \frac{\int_{\Omega_e} N_k(x,y)\,dxdy}{\sum_{i=1}^{nn}\int_{\Omega_e} N_i(x,y)\,dxdy} \\ y_e &= \sum_{k=1}^{nn} H_k \boldsymbol{y}_{n1}^{k\_local} \end{aligned} \tag{7}$$

where nn is the number of nodes that constitute element e, N_k is the interpolation function associated with the local node k of element e. For instance, assuming that the connectivity of an element e is [11, 22, 21, 10], the corresponding local indices are $k = 1, 2, 3, 4$, respectively. In other words, we have: $y_{n1}^{1\_local} \equiv y_{n1}^{11}$, $y_{n1}^{2\_local} \equiv y_{n1}^{22}$, $y_{n1}^{3\_local} \equiv y_{n1}^{21}$, $y_{n1}^{4\_local} \equiv y_{n1}^{10}$.

The two projection steps (P1) and (P2) in Fig. 1 refer to threshold projection function introduced in [38], which projects density values toward 0 or 1 in a manner that depends on the two projection parameters, η and β. The threshold projection function of the step (P1) on an element e is provided in Eq. (8). In Section 3.5, we will show the calculation of the spatial gradient norm in step (NSG) of Fig. 1, which is the step where material-void interfaces are extracted.

$$\phi_e = \frac{\tanh(\beta_1\eta_1) + \tanh(\beta_1(y_e - \eta_1))}{\tanh(\beta_1\eta_1) + \tanh(\beta_1(1-\eta_1))} \tag{8}$$

3.5. Sensitivity analysis

The sensitivity of the objective function (compliance) can be evaluated using the chain rule as follows:

$$\frac{\partial f}{\partial \boldsymbol{z}^e} = \frac{\partial \boldsymbol{y}^j_{\boldsymbol{n}1}}{\partial \boldsymbol{z}^e}\frac{\partial f}{\partial \boldsymbol{y}^j_{\boldsymbol{n}1}}, \tag{9}$$

$$where\ \frac{\partial f}{\partial \boldsymbol{y}^j_{\boldsymbol{n}1}} = \frac{\partial w_{l1}}{\partial \boldsymbol{y}^j_{\boldsymbol{n}1}}\frac{\partial f}{\partial w_{l1}} + \frac{\partial w_{l2}}{\partial \boldsymbol{y}^j_{\boldsymbol{n}1}}\frac{\partial f}{\partial w_{l2}} \tag{10}$$

Recall from Fig. 1 that $\boldsymbol{y}_{\boldsymbol{n}1}$ is the nodal density vector after the first filtering operation (S1). $\boldsymbol{y}^j_{\boldsymbol{n}1}$ is the nodal density variable of node j (global index). $\boldsymbol{z}^e$ is the design variable of element e. The derivatives of compliance with respect to the penalized densities are as shown in [37]:

$$\frac{\partial f}{\partial w_{li}} = -\boldsymbol{U}^T\frac{\partial \boldsymbol{K}}{\partial w_{li}}\boldsymbol{U} = -\boldsymbol{u}_l(\boldsymbol{z})^T\frac{\partial \boldsymbol{k}_l}{\partial w_{li}}\boldsymbol{u}_l(\boldsymbol{z}) \tag{11}$$

The derivative term of the interpolated stiffness on the right side of Eq. (11) is obvious from Eq. (4):

$$\frac{\partial \boldsymbol{k}_l}{\partial w_{li}} = \boldsymbol{k}^0_{li} \tag{12}$$

The rest of the derivative terms on the right side of Eq. (10) are obtained via the chain rule from Eq. (4):

$$\frac{\partial w_{l1}}{\partial \boldsymbol{y}^j_{\boldsymbol{n}1}} = (1-\varepsilon)p\overline{\tau}_l^{p-1}\frac{\partial \overline{\tau}_l}{\partial \boldsymbol{y}^j_{\boldsymbol{n}1}} \tag{13}$$

$$\frac{\partial w_{l2}}{\partial \boldsymbol{y}^j_{\boldsymbol{n}1}} = (1-\varepsilon)p\left[\phi_l^{p-1}\frac{\partial \phi_l}{\partial \boldsymbol{y}^j_{\boldsymbol{n}1}}\left(1-\overline{\tau}_l^p\right) - \phi_l^p\overline{\tau}_l^{p-1}\frac{\partial \overline{\tau}_l}{\partial \boldsymbol{y}^j_{\boldsymbol{n}1}}\right] \tag{14}$$

By the chain rule of partial differentiation again, the two derivative terms on the right side of Eqs. (13) and (14) can be evaluated with the help of the material interpolation process diagram in Fig. 1.

$$\frac{\partial \phi_l}{\partial \boldsymbol{y}^j_{\boldsymbol{n}1}} = \frac{\partial y_e}{\partial \boldsymbol{y}^j_{\boldsymbol{n}1}}\frac{\partial \phi_l}{\partial y_e} \tag{15}$$

$$\frac{\partial \overline{\tau}_l}{\partial \boldsymbol{y}^j_{\boldsymbol{n}1}} = \frac{\partial \phi_e}{\partial \boldsymbol{y}^j_{\boldsymbol{n}1}}\frac{\partial \boldsymbol{y}^k_{\boldsymbol{n}2}}{\partial \phi_e}\frac{\partial \tau_m}{\partial \boldsymbol{y}^k_{\boldsymbol{n}2}}\frac{\partial \overline{\tau}_l}{\partial \tau_m} \tag{16}$$

Terms $\frac{\partial \phi_l}{\partial y_e}$ and $\frac{\partial \overline{\tau}_l}{\partial \tau_m}$ in Eqs. (15) and (16) represent sensitivities related to the threshold projection function [38] and are calculated as follows:

$$\frac{\partial \phi_l}{\partial y_e} = \begin{cases} \dfrac{\beta_1\left[1 - tanh^2(\beta_1(y_e - \eta_1))\right]}{\tanh(\beta_1\eta_1) + \tanh(\beta_1(1-\eta_1))}, & if\ e = l \\ 0, & otherwise \end{cases} \tag{17}$$

$$\frac{\partial \overline{\tau}_l}{\partial \tau_m} = \begin{cases} \dfrac{\beta_2\left[1 - tanh^2(\beta_2(\tau_m - \eta_2))\right]}{\tanh(\beta_2\eta_2) + \tanh(\beta_2(1-\eta_2))}, & if\ m = l \\ 0, & otherwise \end{cases} \tag{18}$$

Note that the parameters $(\eta_i,\ \beta_i)$ used for the two projection steps in Eqs. (17) and (18) correspond to those shown in steps (P1) and (P2) in Fig. 1.

The term $\frac{\partial y_e}{\partial \boldsymbol{y}^j_{n1}}$ in Eq. (15) is related to the mapping step and is evaluated from Eq. (7). Assume the global node index j corresponds to local node index k of element e, then we have:

$$\frac{\partial y_e}{\partial y^j_{n1}} \equiv \frac{\partial y_e}{\partial y^{k\_local}_{n1}} = H_k,\ k = 1, \ldots,\ nn. \tag{19}$$

The term $\frac{\partial \tau_m}{\partial \boldsymbol{y}^k_{n2}}$ in Eq. (16) is related to a combined process of mapping and spatial gradient calculation. The spatial gradient vector of

any element l is expressed as: $\nabla y_{2l} = \begin{pmatrix} \frac{\partial y_{2l}}{\partial x} \\ \frac{\partial y_{2l}}{\partial y} \end{pmatrix}$, where y_{2l} is the second smoothed density of element l. The norm of the spatial gradient vector is:

$$\tau_l = \| \nabla y_{2l} \| = \sqrt{\left(\frac{\partial y_{2l}}{\partial x}\right)^2 + \left(\frac{\partial y_{2l}}{\partial y}\right)^2} \tag{20}$$

The expressions of the spatial gradient components can be derived using Eq. (7) as follows:

$$\begin{aligned} \frac{\partial y_{2l}}{\partial x} &= \sum_{k=1}^{nn} \frac{\partial H_k}{\partial x} \boldsymbol{y}_{n2}^{k\_local} = \frac{1}{const} \sum_{k=1}^{nn} \left(\int_{\Omega_e} \frac{\partial N_k(x,y)}{\partial x} dxdy \right) \boldsymbol{y}_{n2}^{k\_local}, \\ \frac{\partial y_{2l}}{\partial y} &= \sum_{k=1}^{nn} \frac{\partial H_k}{\partial y} \boldsymbol{y}_{n2}^{k\_local} = \frac{1}{const} \sum_{k=1}^{nn} \left(\int_{\Omega_e} \frac{\partial N_k(x,y)}{\partial y} dxdy \right) \boldsymbol{y}_{n2}^{k\_local}, \\ where\ const &= \sum_{i=1}^{nn} \int_{\Omega_e} N_i(x,y) dxdy \end{aligned} \tag{21}$$

Here, the second smoothed nodal densities $\boldsymbol{y}_{n2}$ were considered constant, so we need only calculate the derivatives of the shape functions N_k with respect to spatial variables x and y. The definition of k in Eq. (21) remains to be local node index, same as in Eqs. (7) and (19). Assume a global node index j corresponds to the local node index k of any element, i.e., $\boldsymbol{y}_{n2}^{j} \equiv \boldsymbol{y}_{n2}^{k\_local}$, then its associated shape function is $N_k(x,y)$. The derivative of the gradient norm τ_l of an element l with respect to the nodal density $\boldsymbol{y}_{n2}^{j}$ of a global node j is as follows:

$$\frac{\partial \tau_l}{\partial \boldsymbol{y}_{n2}^{j}} \equiv \frac{\partial \tau_l}{\partial \boldsymbol{y}_{n2}^{k\_local}} = \begin{cases} \frac{1}{const * \tau_l} \left[\frac{\partial y_{2l}}{\partial x} \left(\int_{\Omega_e} \frac{\partial N_k(x,y)}{\partial x} dxdy \right) + \frac{\partial y_{2l}}{\partial y} \left(\int_{\Omega_e} \frac{\partial N_k(x,y)}{\partial y} dxdy \right) \right], & if\ j \in M_l \\ 0, & otherwise \end{cases} \tag{22}$$

where M_l is the set of global indices of the nodes that constitute element l. This derivative is non-zero only if node j constitutes element l. Substitute Eq. (21) into Eq. (22), and we obtain the term $\frac{\partial \tau_m}{\partial \boldsymbol{y}_{n2}^{k}}$ in Eq. (16).

Lastly, the remaining two terms, $\frac{\partial \boldsymbol{y}_{n1}^{j}}{\partial \boldsymbol{z}^{e}}$ in Eq. (9) and $\frac{\partial \boldsymbol{y}_{n2}^{k}}{\partial \phi_e}$ in Eq. (16), are related to the PDE-based density filter. The expressions are directly obtained from the system of linear equations shown in Eq. (6), thus omitted here. Please refer to [34] for detailed expressions.

4. Numerical examples

In this section, five examples of different design domains and/or boundary conditions are discussed. In Sections 4.1 and 4.2, two examples are presented in 2D that use the problem formulation stated in Eq. (1). The examples in Section 4.3 use a more generalized version of the present problem formulation that accommodates multiple local or partial volume constraints. The example explained in Section 4.4 is in 3D. These examples demonstrate several key aspects of the design method of coated structure, such as the ability to accommodate material anisotropy and heterogeneity, the versatility associated to the volume constraint setting, the connection to AM printing processes, among others. Throughout Section 4, the colors red and blue indicate the coating and the bulk materials, respectively. The stopping criterion for convergence is either the maximum number of iterations or the maximum change in design variables with convergence tolerance of 0.01 (whichever is met first). In each example, the initial design variables are set to a value equal to the pre-defined volume fraction limit of the optimization problem.

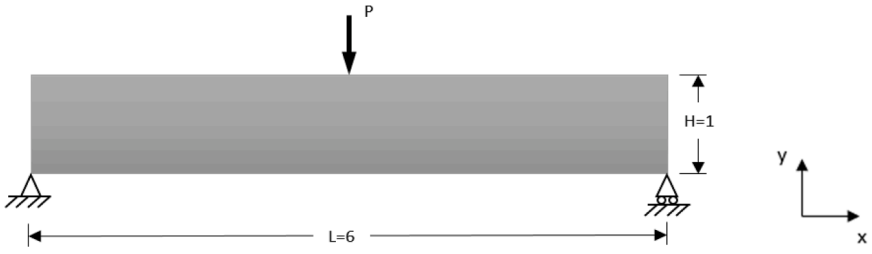

Fig. 4. Design domain and boundary conditions of the 2D MBB beam problem (Section 4.1).

Case #	Directional tensile stiffness	Topology	Objective (f)	Volumes
1	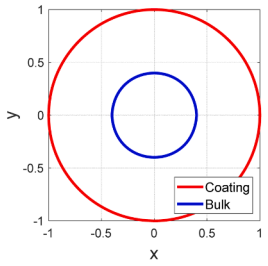	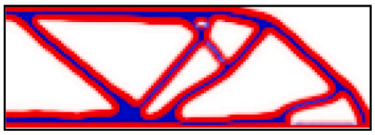	86.233	$V_c = 0.294$ $V_b = 0.106$
2	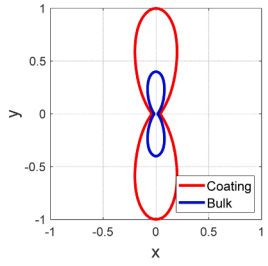	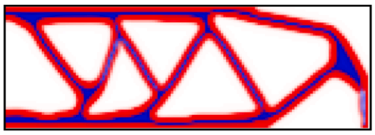	1676.308	$V_c = 0.293$ $V_b = 0.107$
3	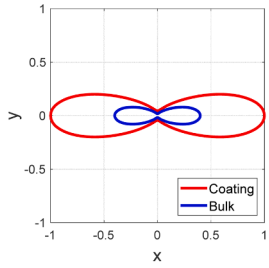	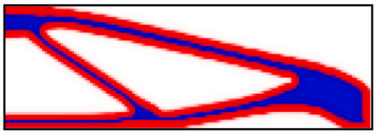	269.86	$V_c = 0.257$ $V_b = 0.143$
4	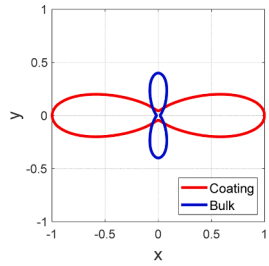	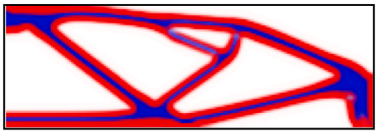	286.31	$V_c = 0.282$ $V_b = 0.118$
5	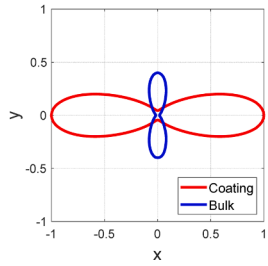	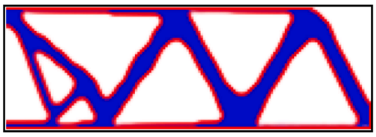	415.6	$V_c = 0.165$ $V_b = 0.235$

Fig. 5. Five MBB beam result cases. Each row provides, for each result case, contour plot of the directional tensile modulus of the coating and the bulk materials, an optimized topology, the optimal objective value $\boldsymbol{f}$ (compliance), and the volume fractions of the coating and the bulk materials (denoted by $\boldsymbol{V_c}$ and $\boldsymbol{V_b}$ respectively) in the final topology. Notice from Table 1 that the filter radii used in case 5 are different than in cases 1–4 (color online).

4.1. 2D MBB beam

First, we consider design of an MBB beam and illustrate how the design is influenced by different combinations of (isotropic and transversely isotropic) materials assigned to the coating and bulk regions. The design domain and boundary conditions of the full MBB beam are provided in Fig. 4, but we consider symmetry boundary conditions at the vertical centerline that allows us to design only the right half of the domain. The magnitude of the load is $P = 1$ for the full beam. The half domain is discretized using 180 by 60 linear quadrilateral finite elements.

Five cases are provided in Fig. 5. In all cases, the prescribed volume fraction limit is $\bar{v} = 0.4$, the maximum directional tensile stiffness of the bulk material is 40% of that of the coating material, and the mass density of the bulk and coating materials are equal (i.e., $\lambda_m = 1$ in Eq. (2)). The design boundary is traced by solid black lines to enhance visualization of the results. Other main optimization parameters are provided in Table 1. To visualize the directionality of the material properties, contour plots showing how the tensile (E_{11}) moduli of the coating and the bulk materials vary with direction are provided for each case, where the 2D stiffness elasticity tensors of both materials are normalized to the largest directional tensile stiffness of the coating material in all cases.

Case 1 is a control case considering an isotropic material for both the coating and the bulk. The coating volume (V_c in Fig. 5) exceeds the bulk volume (V_b in Fig. 5) as reported in Fig. 5. Add to this the fact that the coating material is stiffer than the bulk material, we can assume that the coating material controls the topology more. Nonetheless, the material interpolation process explained in Section 3.2 prevents an "all-coating" design. With both materials isotropic, the solution for case 1 resembles standard solutions for the MBB beam. Case 2 considers two transversely isotropic materials that both have significantly higher tensile stiffness in the vertical direction than in the horizontal. Case 3 considers the same two transversely isotropic materials as case 2, but this time, the tensile stiffness is higher in the horizontal direction than the vertical. In both cases 2 and 3, the coating volume exceeds the bulk volume. Notice, however, that the designs in cases 2 and 3 differ dramatically from the isotropic case 1. Due to high stiffness in the vertical direction, the design obtained for case 2 tends to favor members that are closer to vertical than those in case 1 when possible. Due to high stiffness in the horizontal direction, the design obtained for case 3 tends to favor members that are closer to horizontal than case 1. Notice also that the objective function value (compliance) is sacrificed when considering transversely isotropic materials since they limit design freedom. The objective function in case 3 (high horizontal stiffness) is much lower than the objective function value in case 2 (high vertical stiffness) since horizontal stiffness is more important in resisting deformation in this bending-dominated problem.

In both cases 2 and 3, the coating and the bulk materials shared material directionality, i.e., their axes of cylindrical symmetry as transversely isotropic materials are along the same direction. In case 4, we consider the coating material's stiff axis oriented horizontally and the bulk material's stiff axis to be oriented vertically, but we still enforce that the maximum directional tensile stiffness of the bulk material is 40% of that of the coating. Again, the higher stiffness coating material dominates the design and we observe in Fig. 5 that the case 4 design resembles that of case 3 in that it favors members that are closer to horizontal; however, due to the vertical directional stiffness of the bulk, the case 4 design tolerates members slightly more vertical than in case 3. Note that the objective function value of case 4 lies between that of cases 2 and 3, as expected.

Case 5 shares material properties of the coating and the bulk materials with those of case 4, but we reduce the thickness of the coating region by modifying the filter radii of the two smoothing operations (see Table 1) so that the coating is thinner in case 5 than in case 4. In case 5, the truss members connecting the top and bottom of the MBB beam are more vertically oriented than those in case 4 since we have indirectly restricted the allowable volume of coating material via the filter radii. Therefore, although the bulk material is less stiff, its vertically dominant directional stiffness dictates the vertically-biased orientation of members in the final design. Further, we observe in the topology of case 5 that most bulk material resides in the more vertically oriented truss members while the horizontal members at the top and the bottom contain little bulk material since bulk material does not contribute much to the horizontal stiffness needed in these regions. As a result, the horizontal members are much thinner than the slanted members.

4.2. 2D curved beam

An interesting type of design domain would include an arch shape as part of the design boundary. Consider the curved beam problem presented in Fig. 6 with dimensional parameters $H = 1.25$, $L = 2$, $c_1 = (x_{c1}, y_{c1}, r_{c1}) = (0,\ 0,\ 1.5)$, $c_3 = (0,\ 0.25,\ 0.5)$, c_1 and c_3 contain the center coordinates and radii of the two arcs. This curved beam problem is modified from an example in [35]. The curved beam is fixed on the two sides and is subjected to loadings on the arc c_3. The five loads have equal magnitude $P = 1$, are evenly spaced and oriented 30° with each other. Using `PolyMesher`, a polygonal finite element mesh generator [39], the domain is discretized into

Table 1
Optimization parameters used for the MBB beam problem (brackets indicate continuation).

Filter radii of result cases 1–4	$R_1 = 0.15,\ R_2 = 0.08$.
Filter radii of result case 5	$R_1 = 0.15,\ R_2 = 0.03$.
SIMP penalty parameter, p	[1, 2, 3, 4]
Threshold projection parameter, β_1	[1, 5, 10, 15]
Threshold projection parameter, β_2	[8, 8, 8, 10]
Max. number of iterations (per continuation step)	120

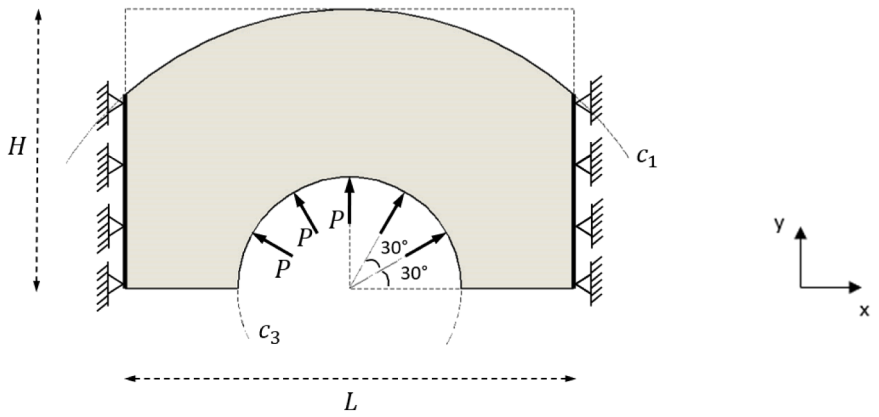

Fig. 6. Design domain and boundary conditions of the curved beam problem of Section 4.2.

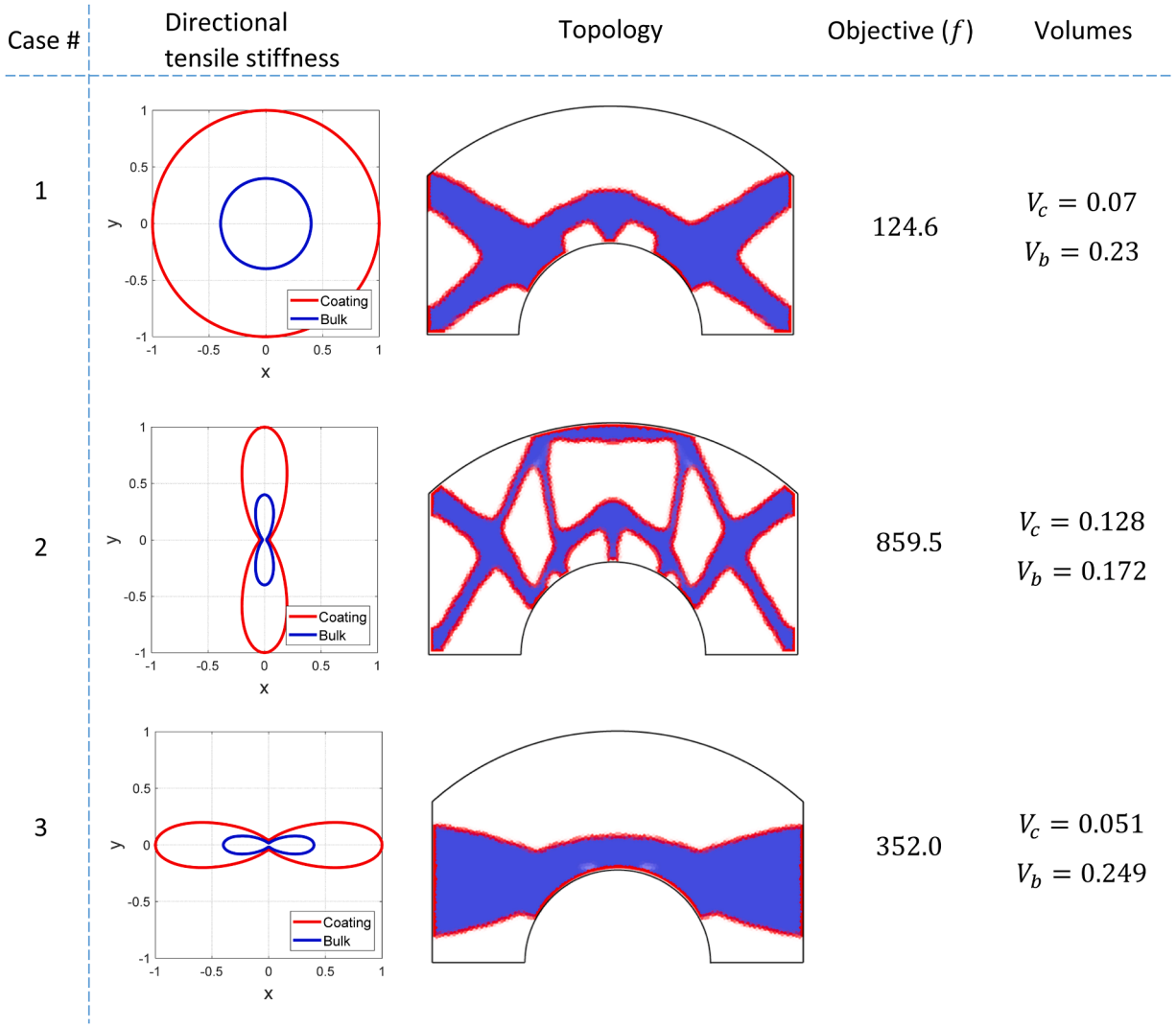

Fig. 7. Three curved beam results. Each row provides, for each result case, contour plot of the directional tensile modulus ($\boldsymbol{E}_{11}$) of the coating and the bulk materials, an optimized topology, the optimal objective value $\boldsymbol{f}$ (compliance), and the volume fractions of the coating and the bulk materials (denoted by $\boldsymbol{V_c}$ and $\boldsymbol{V_b}$ respectively) in the final topology (color online).

7500 polygonal elements with symmetry enforced about the vertical y-axis. Three result cases are provided, the material properties of which are the same as those used in the cases 1–3 of the MBB beam problem (in Section 4.1) respectively, as reported in Fig. 7. The prescribed volume fraction limit is $\bar{v} = 0.3$ for all three cases, the filter radii are $R_1 = 0.1,\ R_2 = 0.02$. All other optimization parameter values have the same values as defined in Section 4.1.

In the optimized topologies presented in Fig. 7, the solid black lines trace the design boundary. Similar to the MBB beam, we observe that topology (or the orientation of truss-like members) follows the stiffest tensile direction in each case. Truss-like members in the case 2 design are thinner and more vertically oriented than the trusses in case 1 design, because the materials in case 2 have the stiffest tensile moduli in the vertical Y-axis and thus, case 2 requires more coating material (which is stiffer) to resist bending. The topology of case 3 has fewer truss members than case 1; it looks bulkier and more streamlined from the support to the loading regions, which requires less coating material. This is due to high stiffness in the horizontal direction of the materials. Again, the objective value (compliance) is sacrificed when considering anisotropic materials.

4.3. A more general setting for volume constraints

The problem formulation in Eq. (1) allows for one global volume constraint which controls both the coating and the bulk materials. In other words, the volume constraint limits the sum of the interpolated volumes of the two materials to occupy no more than $\bar{v}$ (the prescribed volume fraction limit) of the total domain volume. In this subsection, we will use two examples to demonstrate that the coated structure design method can also accommodate multiple local or partial volume constraints using a slightly modified problem formulation that is provided in Eq. (23):

$$\begin{aligned} &\min_{z_1,\ldots,z_n} f = \boldsymbol{F}^T \boldsymbol{U}(\boldsymbol{z}) \\ &\textit{subjected to}: \quad g_j = \frac{\sum_{i\in \mathrm{M}_j}\sum_{l\in \mathrm{E}_j} A_l m_V^i(y_l)}{\sum_{l\in \mathrm{E}_j} A_l} - \bar{v}_j \le 0, \quad j = 1,\ldots,k \\ &\text{with}: \quad \boldsymbol{K}(\boldsymbol{z})\boldsymbol{U}(\boldsymbol{z}) = \boldsymbol{F} \end{aligned} \tag{23}$$

g_j is the function that describes the volume constraint j, in which M_j is the set of material indices associated with constraint j, and E_j is the set of element indices associated with constraint j. Recall from Eq. (1) that m_V represents a volume interpolation function of the smoothed density y_l of element l. We assume an element l is associated with the constraint g_j. For the design of coated structure, there exist three possibilities for the material set M_j. If $\mathrm{M}_j = \{1\}$, it means only the coating material is associated with constraint j, then $m_V^i(y_l) \equiv\ m_V^1(y_l) = \overline{\tau}_l$. If $\mathrm{M}_j = \{2\}$, it means only the bulk material is associated with constraint j, then $m_V^i(y_l) \equiv\ m_V^2(y_l) = \lambda_m \phi_l (1 - \overline{\tau}_l)$. If $\mathrm{M}_j = \{1,\ 2\}$, it means both materials are associated with constraint j, then $m_V^i(y_l) = V_l$, the expression of which is in Eq. (2). The above expressions of $m_V^i(y_l)$ were obtained by separating the volume interpolation functions of the two materials.

Next, we will discuss two types of local volume constraints. In Section 4.3.1, we define a partial volume constraint associated with a single material and apply it on a curved beam problem, and observe the differences in the results from a global volume-constrained optimization. In Section 4.3.2, we define multiple local constraints that control both materials, and demonstrate the effect using a serpentine-shaped beam problem.

4.3.1. Partial constraint

Since the volume of the coating material is dependent on the filter radii of the smoothing operations, one idea is to associate only the bulk material with a volume constraint and let the coating material form freely at the material interfaces. We refer to this as a

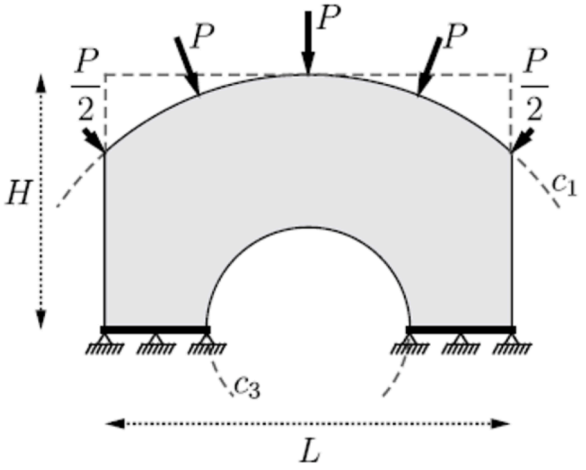

Fig. 8. Design domain and boundary conditions of the curved beam problem of Section 4.3.1 (figure adapted from [35]).

partial constraint. We use the curved beam presented in Section 4.2, with a different set of boundary conditions, as displayed in Fig. 8, which is an adaptation from [35]. For this problem in Fig. 8, one volume constraint is defined to control the bulk material over the entire design domain. The associated material and element indices as defined in Eq. (23) are then $\mathrm{M} = \{2\}$ and $\mathrm{E} = \{1, \ldots, n\}$ respectively, where n is the number of elements. Same as in Section 4.2, the domain is discretized into 7500 polygonal elements with a vertical line of symmetry.

We first used isotropic materials and defined the volume fraction limit of the bulk material $\bar{v}_b = 0.1$. Using the main optimization parameters provided in Table 2, we obtain an optimized topology as shown in Fig. 9(a), in which the design boundary is traced by solid black lines. Volume fractions of the coating and the bulk materials are 0.163 and 0.1 respectively in this solution as reported in Fig. 9 (a), which indicates the partial volume constraint on the bulk material is active.

Knowing that the total volume fraction is 0.263 at convergence, we designed another coated structure of the same curved beam problem, this time using the formulation in Eq. (1), in which the global volume constraint has a prescribed limit of $\bar{v} = 0.263$; all other parameters are the same as defined in Table 2. Note that no continuation was applied to the projection parameter β_2, as $\beta_2 = 8$ was sufficient to produce effective results. The result of this global volume constrained optimization is shown in Fig. 9(b). We will explore the effect of applying a partial volume constraint versus a global constraint, by comparing these two structures which have the same total material volume at convergence, but one obtained from controlling only the bulk material (Fig. 9(a)), the other obtained from controlling the sum of the two materials (Fig. 9(b)).

We observe that the result in Fig. 9(a) has more complexities than Fig. 9(b), with a sparser and more even distribution of material across the design domain, which is consistent with the fact that the coating volume in Fig. 9(a) is more than double that in Fig. 9(b). In contrast, Fig. 9(b) shows thicker truss members, with most of the material located in specific regions. For example, in Fig. 9(b), there is no material present toward the center (or the vertical centerline) of the design domain, whereas Fig. 9(a) has thin solid members extending into the central area.

It is interesting that the objective value of the global volume constrained minimization (shown in Fig. 9(b)) is lower despite the lower amount of the coating material used; recall that the coating material is stiffer than the bulk material. The difference between cases (a) and (b) of Fig. 9 lies in the volume constraint definition: In case (a), a partial volume constraint is applied, fixing the amount of the bulk material, while the coating material can adjust its volume as needed at the material interfaces. In contrast, case (b) applies a global volume constraint, allowing the two materials to distribute the material volume amongst themselves, as long as the total material volume does not exceed a certain limit. Although these two designs use the same total amount of materials, case (b) allows greater flexibility in how the material is allocated between the coating and bulk materials. In other words, case (b) is less restrictive on choosing the proportion of the bulk with respect to the coating materials used in the design, which leads to a lower objective in case (b). This example illustrates that for a coated structure, the finding commonly observed in multi-material topology optimization, that using a larger amount of the stiffer material usually leads to a stiffer structure, does not necessarily hold true or apply in a straightforward manner.

Next, we consider two transversely isotropic materials that both have significantly higher tensile stiffness in the vertical direction than in the horizontal. Symbol λ_D denotes the ratio of the elasticity tensor of the bulk material relative to the coating material, which is analogous to the scale factor λ_E of the isotropic case (used in Eq. (3)). To obtain different values of λ_D and observe its effect on the results, normalized properties of the coating material remain unchanged while those of the bulk material are varied, as shown in Fig. 10. For each λ_D value, two compliance minimization problems on the curved beam (shown in Fig. 8) are conducted in sequence: The first one is subjected to a partial volume constraint that limits the bulk material to occupy no more than $\bar{v}_b = 0.25$ of the total domain volume. The total volume fraction of the two materials, denoted by v_{tt}, is obtained from this solution, then inputted into the second minimization problem as the prescribed volume fraction limiting the sum of the coating and bulk materials. Note that in both minimization problems, volume constraints are associated with all the elements in the design domain. We refer to these two minimization problems as "Calc #1″ and "Calc #2″ respectively, the results of which are provided for each λ_D value. Results of "Calc #1″ and "Calc #2″ are stored in columns (a) and (b), respectively, in Fig. 11 and in Table 3. We first choose to generate relatively thin coating region using filter radii $R_1 = 0.1,\ R_2 = 0.02$. The mass density of the bulk material is the same as the coating material, i.e., $\lambda_m = 1$ in Eq. (2).

Table 3 column (c) verifies that for each λ_D value, the total material volumes of the two optimization problems (Calc #1 and Calc #2) are kept the same (v_{tt}). Columns (a) (i.e., the Calc #1 results) reveal that as the ratio λ_D increases, the volume fraction of the coating material decreases while that of the bulk material remains 0.25 (indicating an active partial volume constraint). Since the relative stiffness of the bulk material increases with λ_D, the amount of bulk material that the optimizer chooses to use would naturally increase

Table 2
Optimization parameters used for the curved beam problem in Section 4.3.1 (brackets indicate continuation).

Number of elements	7500
Filter radii	$R_1 = 0.1,\ R_2 = 0.02.$
Relative mass density (refer to Eq. (2))	$\lambda_m = 0.7$
Relative Young's modulus (refer to Eq. (3))	$\lambda_E = 0.4$
SIMP penalty parameter, p	[1, 2, 3, 4]
Threshold projection parameter, β_1	[1, 5, 10, 15]
Threshold projection parameter, β_2	[8, 8, 8, 8]
Max. number of iterations (per continuation step)	120

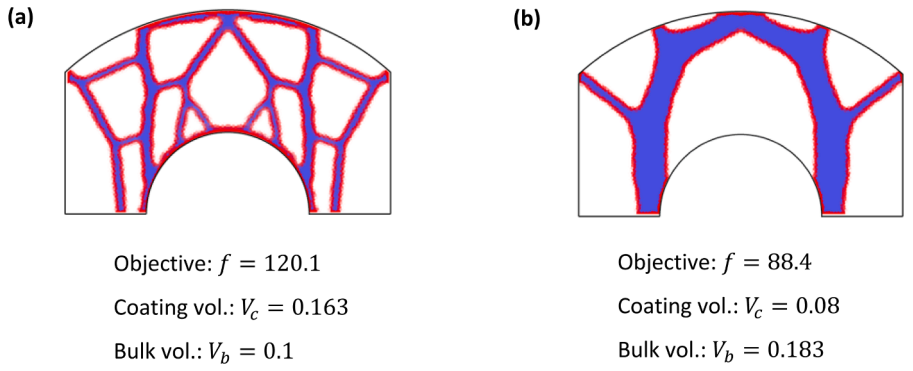

Fig. 9. Curved beam optimized for: (a) a partial volume constraint ($\overline{\boldsymbol{v}}_{\boldsymbol{b}} = 0.1$) controlling only the bulk material in the entire domain; (b) a global constraint ($\overline{\boldsymbol{v}} = 0.263$) controlling all materials in the entire domain. The total volume fractions of the two results are kept the same. Each result provides the objective value $\boldsymbol{f}$ (compliance) and the volume fractions of the coating and the bulk materials (denoted by $\boldsymbol{V_c}$ and $\boldsymbol{V_b}$ respectively) in the final topology (color online).

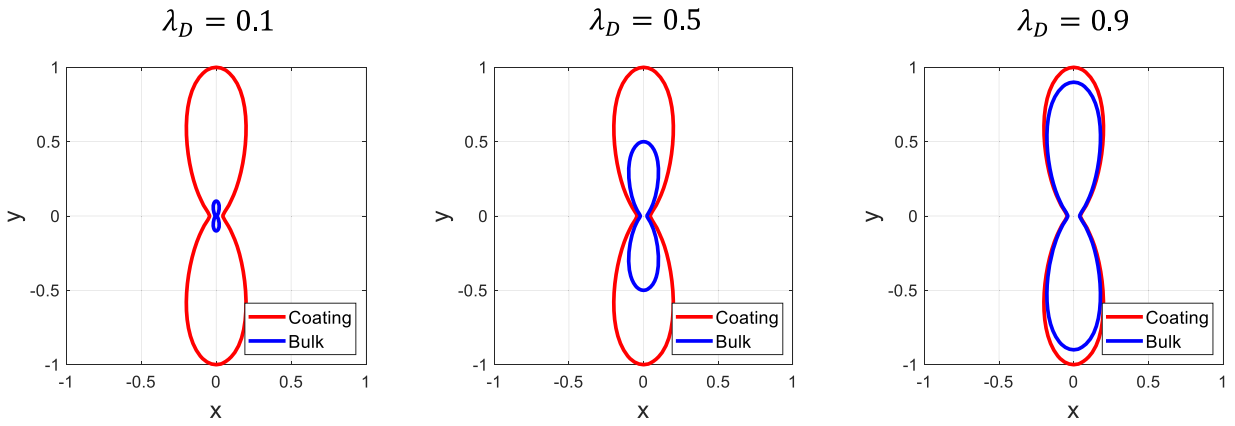

Fig. 10. Contour plots of the directional tensile moduli of the coating and the bulk materials for three different values of the ratio λ_D (color online).

relative to the coating material. This is reflected in the topologies corresponding to the first minimization problem (in column (a) in Fig. 11): As λ_D increases, fewer and fewer complexities exist in the topology, which results in less and less coating region.

Columns (b) (i.e., the Calc #2 results) in Table 3 display an overall increase in the usage of bulk material in the second optimization ("Calc #2″) compared to the first ("Calc #1″), except the case of $\lambda_D = 0.1$ in which the volume fraction of the bulk material reduced slightly (by 0.001). This is consistent with the results provided in Fig. 11, in which solutions of the second optimization ("Calc #2″ in column b) contain fewer details (e.g., fewer enclosed voids) than those of the first optimization ("Calc #1″ in column a), for the cases $\lambda_D = 0.5$ and $\lambda_D = 0.9$ in particular. As much as the optimizer wants to favor the coating material as it is stiffer, the coating material cannot be used freely even under a global volume constraint, because it is only applied at the material-void interfaces. Not a lot of coating is needed in this case because we chose filter radii that produce relatively thin coating. Column (d) in Table 3 reveals that the percentage of coating that was turned to bulk material at the second minimization problem ("Calc #2″) increases with ratio λ_D. In the case of $\lambda_D = 0.9$ in which the two materials' directional tensile stiffness become very close, only $\frac{0.071}{0.36} = 19.72\%$ of the coating material occupies the total material volume in the solution of the global volume constrained minimization problem.

Comparing the two columns in Fig. 11, we observe that the second optimization (column (b), or Calc #2) produces a more optimal result than the first (column (a), or Calc #1) for any λ_D value. There exist thin truss-like members in the solutions of the first optimization displayed in column (a) that connect all the loading points along the circular boundary at the top. These members may have contributed to more usage of the coating material but less optimal topologies. We can see these members were removed in the results of the second optimization displayed in column (b).

We then used a different set of filter radii $R_1 = 0.15,\ R_2 = 0.08$ to generate a relatively thick coating. The three sets of material properties and all other parameters remain unchanged. Results are presented in Fig. 12 and Table 4.

Observation on the material volume data in Table 4 is overall consistent with that from Table 3, except two details: First, the bulk volume is smaller than $\overline{v} = 0.25$ in the solution of the first optimization shown in columns (a) in the case of $\lambda_D = 0.1$, indicating a non-active partial constraint. A thicker coating region provides the necessary amount of coating material such that an optimized topology does not require a bulk volume as large as 0.25, as the bulk material is much less stiff than the coating. Second, all percentages in

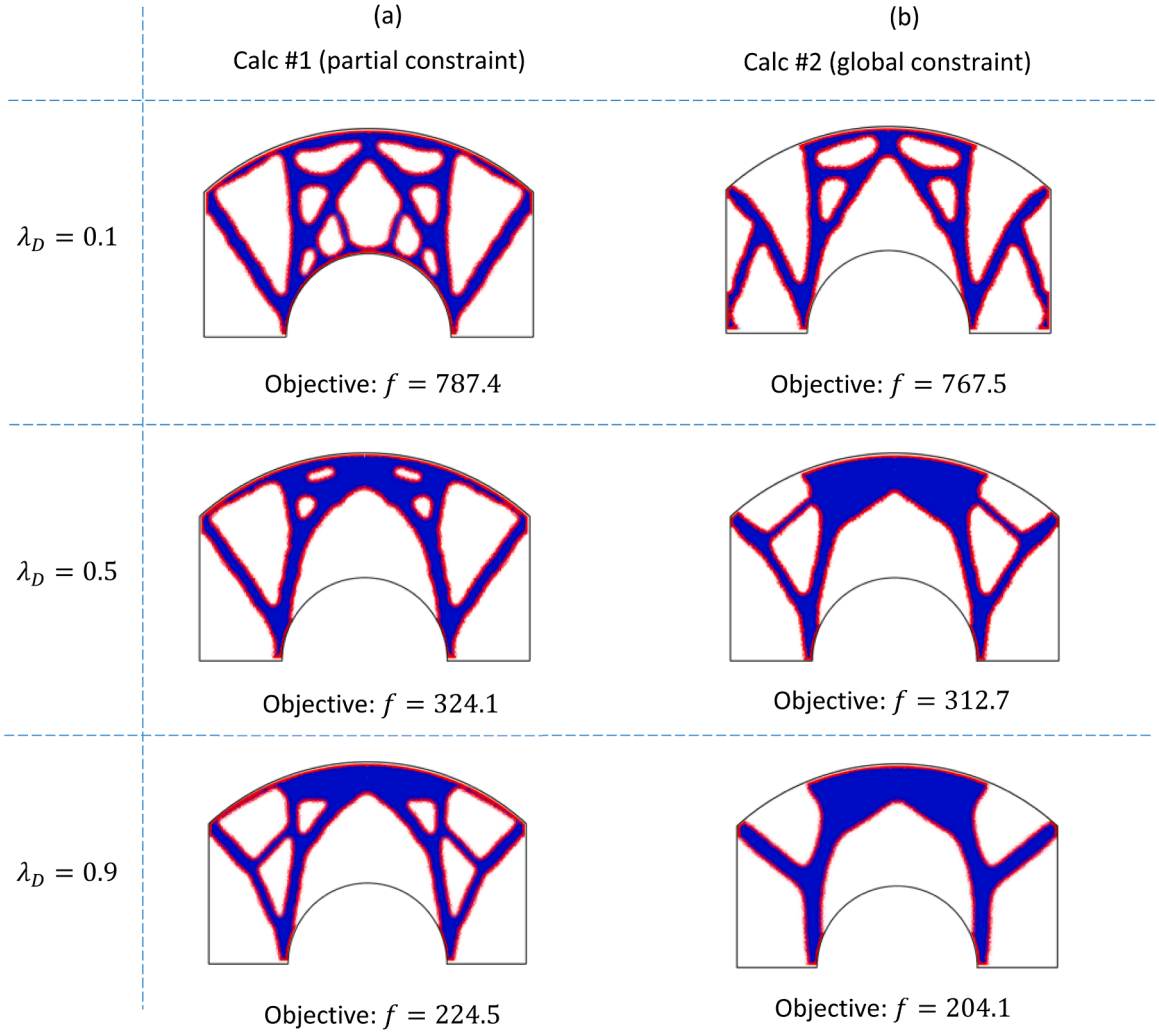

Fig. 11. Curved beam results obtained using a relatively thin coating ($\boldsymbol{R}_1 = 0.1,\ \boldsymbol{R}_2 = 0.02$). Columns (a) and (b) provide the optimized topologies and their corresponding objective values of the two minimization problems (referred to as "Calc #1″ and "Calc #2″), respectively, for each $\boldsymbol{\lambda_D}$ case (color online).

Table 3
Curved beam results obtained using a relatively thin coating ($R_1 = 0.1,\ R_2 = 0.02$): Columns (a) and (b) of the table record respective volume fractions of the coating and the bulk materials in the solutions of the two minimization problems (referred to as "Calc #1″ and "Calc #2″). Column (c) provides the total volume fraction (v_{tt}) of coating and bulk materials for each λ_D value. Column (d) records the increase of bulk material volume in the second optimization ("Calc #2″) compared to the first ("Calc #1″).

	(a) Calc #1 (partial constraint)		(b) Calc #2 (global constraint)		(c) Total volume fraction (v_{tt})	(d) Volume increase in bulk material relative to total volume fraction
	Coating vol.	Bulk vol.	Coating vol.	Bulk vol.		
$\lambda_D = 0.1$	0.14	0.25	0.141	0.249	0.39	-0.26%
$\lambda_D = 0.5$	0.12	0.25	0.095	0.275	0.37	6.76%
$\lambda_D = 0.9$	0.11	0.25	0.071	0.289	0.36	10.83%

column (d) are positive, indicating a consistent increase in the usage of bulk material in the global volume constrained optimization (i.e., Calc #2) compared to the partial constrained optimization (i.e., Calc #1) for any λ_D.

Observing the results in Fig. 12, one difference from Fig. 11 is that objective value of the Calc #2 result is higher than the Calc #1 result in the case of $\lambda_D = 0.1$. Differences in the objective values between the two minimization problems are smaller than those

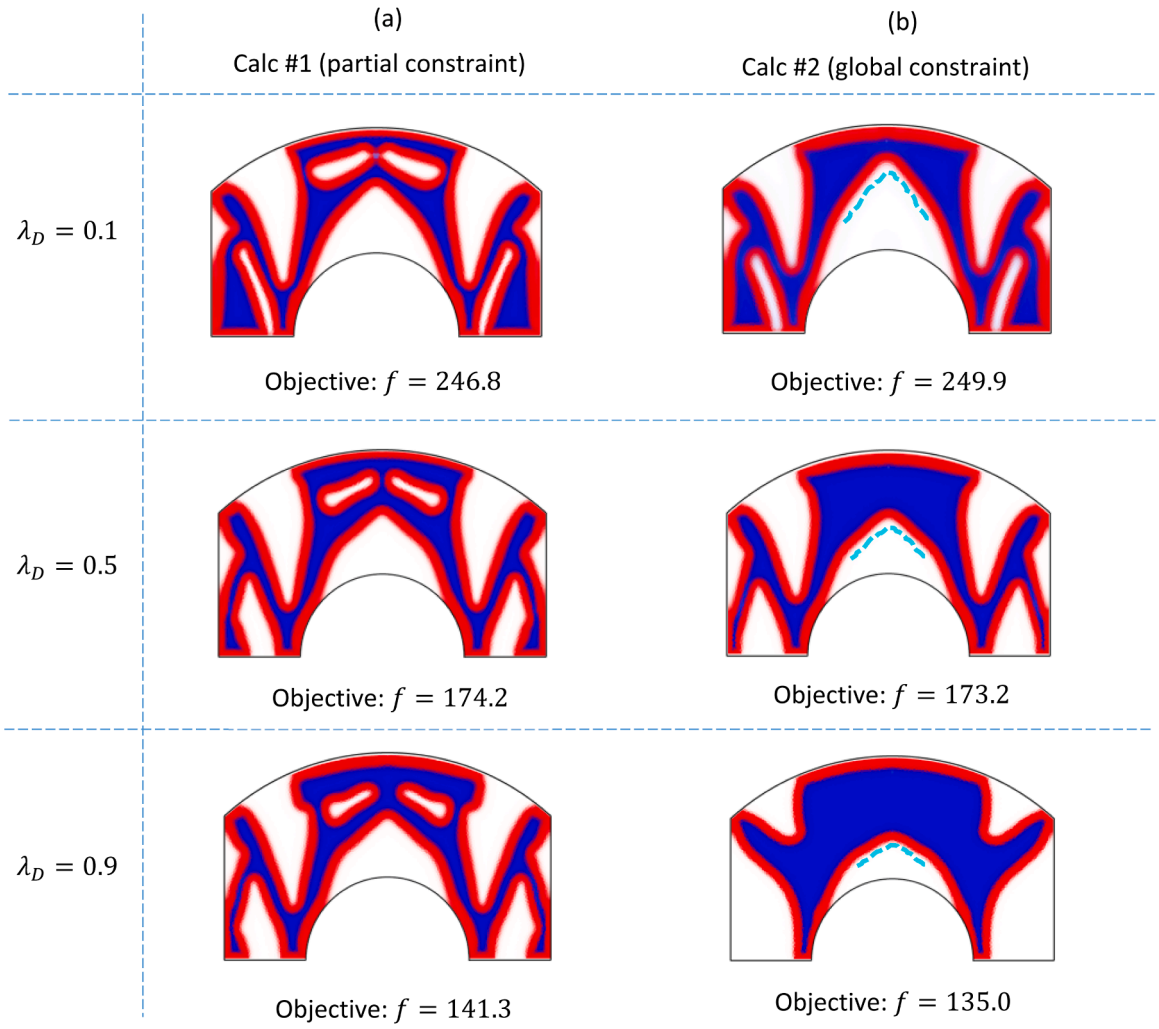

Fig. 12. Curved beam results obtained using a relatively thick coating ($\boldsymbol{R}_1 = 0.15$, $\boldsymbol{R}_2 = 0.08$). Columns (a) and (b) provide the optimized topologies and their corresponding objective values of the two minimization problems (referred to as "Calc #1″ and "Calc #2″), respectively, for each $\boldsymbol{\lambda_D}$ case. The dashed cyan lines in the results in column (b) indicate the change in steepness of the overhanging region in the optimized topologies of the second minimization problem (color online).

Table 4
Curved beam results obtained using a relatively thick coating ($R_1 = 0.15$, $R_2 = 0.08$): Columns (a) and (b) of the table record respective volume fractions of the coating and the bulk materials in the solutions of the two minimization problems (referred to as "Calc #1″ and "Calc #2″). Column (c) provides the total volume fraction (v_{tt}) of coating and bulk materials for each λ_D value. Column (d) records the increase of bulk material volume in the second optimization ("Calc #2″) compared to the first ("Calc #1″).

	(a) Calc #1 (partial constraint)		(b) Calc #2 (global constraint)		(c) Total volume fraction (v_{tt})	(d) Volume increase in bulk material relative to total volume fraction
	Coating vol.	Bulk vol.	Coating vol.	Bulk vol.		
$\lambda_D = 0.1$	0.415	0.243	0.397	0.261	0.658	2.74%
$\lambda_D = 0.5$	0.395	0.25	0.332	0.313	0.645	9.77%
$\lambda_D = 0.9$	0.393	0.25	0.218	0.425	0.643	27.22%

obtained using the thinner coating. Solutions between the two minimization problems are similar except that enclosed voids exist in the topologies of the first minimization provided in column (a), which require more coating volume. As λ_D increases, steepness of the overhanging region traced by dashed cyan lines in the topologies in column (b) (Calc #2) decreases. This is consistent with the more

and more bulk material usage as the stiffness of bulk material increases. In the solutions of both minimization problems, truss-like members that are directly connected to the fixed edges at the bottom of the design space are the thickest in the case of $\lambda_D = 0.1$, then become thinner as λ_D increases. These members have an almost vertical orientation and transfer loads to the support. As the bulk material becomes stiffer, thick truss members are less needed at the support.

4.3.2. Local constraints

Another type of volume constraint that can be specified with Eq. (23) are local constraints, each of which controls both the coating and the bulk materials in a sub-region of the design domain. The associated material and element indices of a local constraint j are $\mathrm{M}_j = \{1, 2\}$ and $\mathrm{E}_j \in \{1, \ldots, n\}$ respectively. We will only consider isotropic materials in this sub-section. Consider the serpentine-shaped beam problem shown in Fig. 13 that is borrowed from [35]. For more information on the domain geometry and boundary conditions, please refer to [35]. The domain is divided into 84 sub-regions, each sub-region is bounded by dashed lines and/or the design boundary. The volume fraction limits are $\bar{v}_j = 0.5,\ j = 1,\ldots,84$, which means the total volume of the two materials is limited to occupy no more than 50% of each sub-region. Other main parameters are provided in Table 5.

Fig. 14(b) shows an optimized topology of this local volume constrained optimization (which has 84 local volume constraints). The dashed lines trace the design boundary. We compare it with Fig. 14(a), a coated result of the same problem optimized for a single global volume constraint, the prescribed volume fraction limit of which is $\bar{v} = 0.5$. Note that the total material volume of the two designs is the same. In the solution of the local volume constrained optimization (Fig. 14(b)), material is more evenly distributed over the design domain, with finer details near the fixed edge. Truss-like members are less bulky at the top and bottom of the design boundary compared to the design in Fig. 14(a), which results in a higher coating volume in Fig. 14(b). The solution demonstrates the coated structure's ability to smoothly transition from smaller to larger sub-regions that are associated with the same volume fraction limit. The coating layer is smoothly connected between sub-regions of different sizes, and coating thickness is consistent throughout the design domain. As expected, the design with more constraints (Fig. 14(b)) has a higher objective value, despite the higher usage of coating material (which is the stiffer of the two materials).

4.4. 3D cantilever beam

The design approach presented in this work is implemented on a 3D cantilever beam. The domain and boundary conditions are provided in Fig. 15, where the length parameter $L = 1$, and the load $P = 1$. The beam is fixed on the left face at the two shaded areas and loaded vertically at the central point on the right face. The domain is discretized into $93 \times 31 \times 31 = 89373$ eight-node hexahedral elements.

We first investigate the effect of material directionality by comparing two cases that are provided in Fig. 16. Case #1 considers two transversely isotropic materials that both have significantly higher tensile stiffness in the horizontal direction than in the vertical direction. Case #2 considers the same two transversely isotropic materials as case #1, but this time, the tensile stiffness is higher in the vertical direction than the horizontal direction. A surface plot is provided for each case that shows how the normalized tensile modulus (E_{11}) of the coating material varies with the direction. The magnitude of the tensile modulus along any direction is displayed on a color scale shown at the bottom of Fig. 16. The surface plots of the bulk material are omitted as its maximum tensile stiffness is 40% of the coating material. In both cases, the prescribed volume fraction limit is $\bar{v} = 0.4$, the filter radii are $R_1 = 0.15,\ R_2 = 0.08$. Other main parameters are given in Table 6, which remain unchanged throughout this 3D example.

The optimized design of case #1 presents more material on the front and back sides of the cantilever, forming two walls that merge at the loading region. Distinct from that in case #1, the design in case #2 has most of its material at the top and bottom faces of the cantilever. Except near the support and loading regions, its YZ cross sectional views resemble a wide-flange beam or an I-beam such as shown in Fig. 17, which is the density field of the cross section at $X = 1.77$. This design aligns with the material directionality of case #2: Tensile (or compressive) stresses reach their maximum at the top (or bottom) of a cross section of the beam in this bending-dominated problem. Since the tensile moduli of both materials are very low in the beam's lengthwise direction (X-axis) in case #2, it is reasonable that the optimizer places a lot of material at these critical areas to resist bending. Nonetheless, the low stiffness in the horizontal direction still resulted in a much higher objective value in case #2 than in case #1.

In addition to material directionality, let us investigate the effect of a few other parameters on the results. Three cases are provided

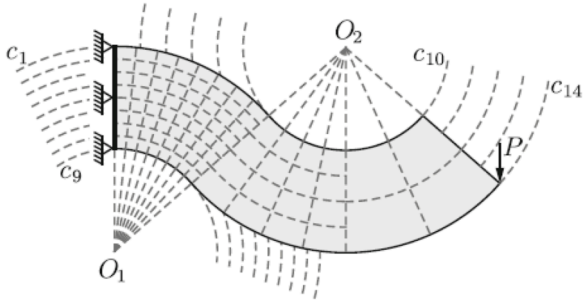

Fig. 13. Domain and boundary conditions of the serpentine problem of Section 4.3.2 (figure borrowed from [35]).

Table 5
Optimization parameters used for the serpentine problem.

Number of elements	50,000
Filter radii	$R_1 = 0.1,\ R_2 = 0.04.$
Relative mass density (refer to Eq. (2))	$\lambda_m = 1$
Relative Young's modulus (refer to Eq. (3))	$\lambda_E = 0.4$
SIMP penalty parameter, p	$[1,\ 2,\ 2.5,\ 3,\ 4]$
Threshold projection parameter, β_1	$[1,\ 5,\ 8,\ 10,\ 12]$
Threshold projection parameter, β_2	$[8,\ 8,\ 8,\ 8,\ 8]$
Max. number of iterations (per continuation step)	150

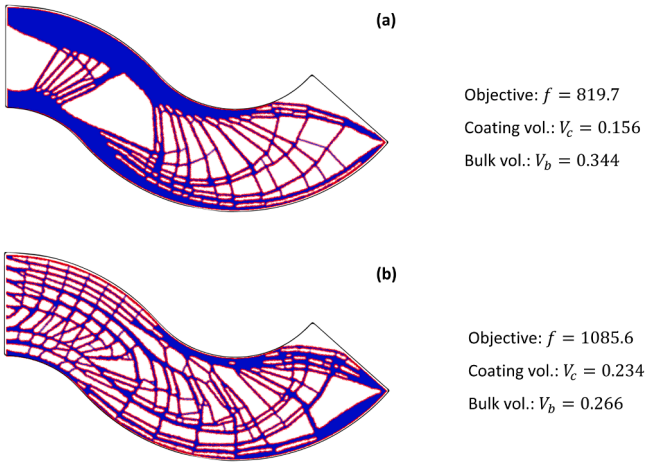

Fig. 14. Coated designs of serpentine beams: (a) a single global volume constraint controlling both materials in the entire domain; (b) 84 local constraints, each controlling both materials in a sub-region of the domain. The sub-regions are illustrated in Fig. 13. Also provided for each case are the objective value $\boldsymbol{f}$ (compliance) and the volume fractions of the coating and the bulk materials (denoted by $\boldsymbol{V_c}$ and $\boldsymbol{V_b}$ respectively) in the final topology (color online).

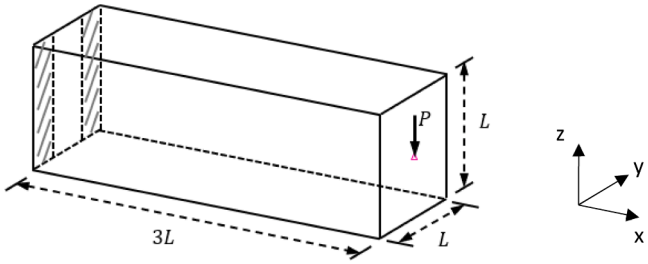

Fig. 15. Design domain and boundary conditions of the 3D cantilever beam problem.

in Fig. 18: between cases (a) and (b), a smaller filter radius R_2 is used in case (a); between cases (b) and (c), the prescribed volume fraction limit $\bar{v}$ used in case (c) is half of that in case (b). All cases use the material properties of case 1 shown in Fig. 16 (i.e., significantly higher tensile stiffness in the horizontal direction). The parameters of interest ($\bar{v},\ R_1,\ R_2$) are provided for each case in Fig. 18. Comparing between cases (a) and (b), the solution in Fig. 18(a) looks bulkier and less streamlined from the support to the loading point than that in Fig. 18(b). The opening between the front and back sides of the cantilever is shallower in case (a). A smaller filter radius R_2 generates a thinner coating in case (a), which results in a lower coating volume than in case (b) as provided in Fig. 18; since the coating material is stiffer, the design in case (a) requires bulkier structure close to the support and the loading regions to transfer load. The objective value of case (a) is higher than case (b) for the same reason. Comparing between cases (b) and (c), the objective of case (c) is naturally much higher than case (b) with only half the prescribed volume fraction $\bar{v}$. The opening between the front and back sides of the cantilever in the solution of case (c) is wider and deeper, producing a thinner structure.

Since only the coating layer can be seen from the outside of a 3D coated structure, we provide YZ cross-sectional views of the above three cases at $X = 1.29$ and $X = 1.77$ respectively in Fig. 19. It can be verified in each section view that the bulk material (in blue) is enclosed by the coating (in red). The filters cause mixing at the interface between the coating and bulk materials. The length scale of the mixing region observed in the final design could be decreased by refining the mesh. Comparing between cases (a) and (b), the

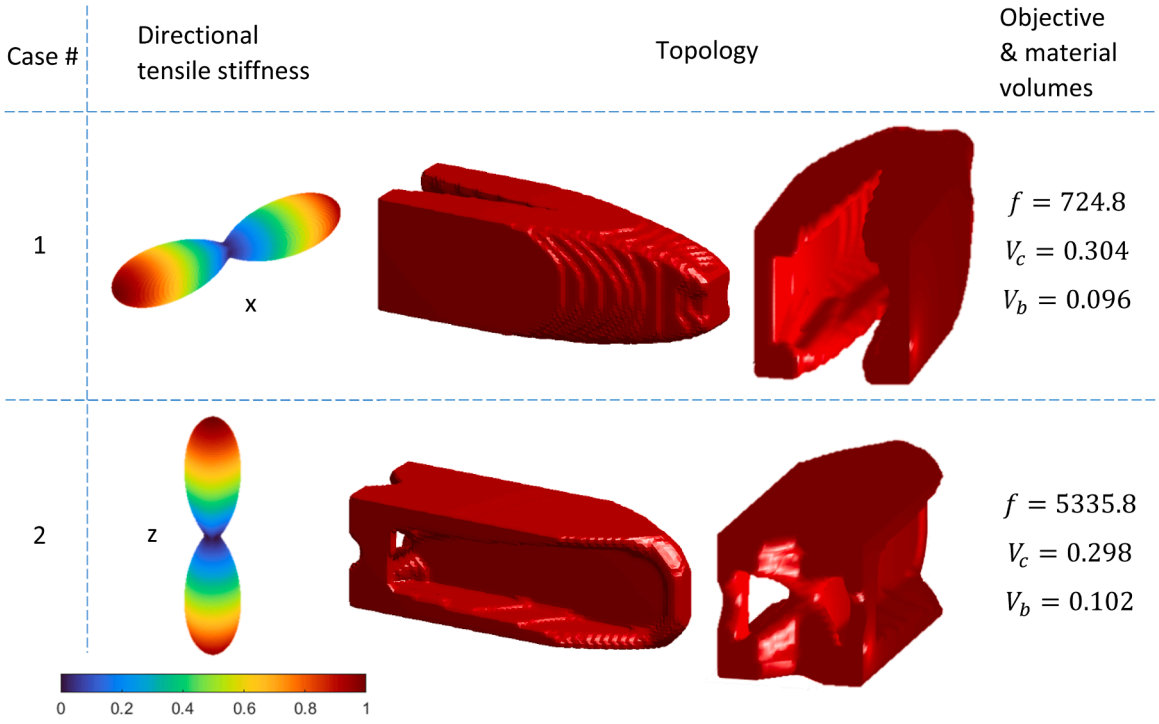

Fig. 16. Two cantilever beam result cases. Each row provides, for each result case, surface plot of the normalized directional tensile modulus of the coating material, an optimized topology presented in two isometric views, the optimal objective value $\boldsymbol{f}$ (compliance), and the volume fractions of the coating and the bulk materials (denoted by $\boldsymbol{V_c}$ and $\boldsymbol{V_b}$ respectively) in the final topology (color online).

Table 6
Values of the optimization parameters that remain constant throughout the 3D cantilever beam problem.

Number of elements	89,373
Relative mass density (refer to Eq. (2))	$\lambda_m = 0.7$
Relative stiffness tensor	$\lambda_D = 0.4$
SIMP penalty parameter, p	[1, 2, 3, 4]
Threshold projection parameter, β_1	[1, 5, 10, 15]
Threshold projection parameter, β_2	[8, 8, 8, 8]
Max. number of iterations (per continuation step)	120

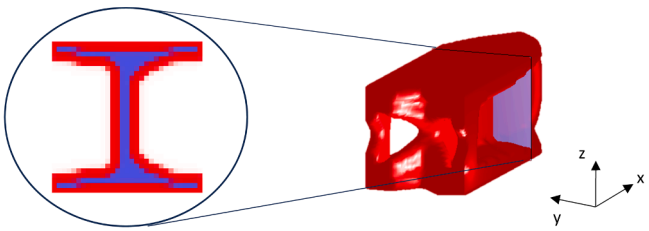

Fig. 17. An illustration (drawn using TOPslicer [40]) showing a zoomed-in YZ cross section at $\boldsymbol{X} = 1.77$ of the case #2 design shown in Fig. 16 (color online).

coating in the section views of case (b) is visibly thicker than that of case (a), which makes the structure in case (b) stiffer. The cross section of case (b) at $X = 1.29$ is split by a small opening in the middle as observed in Fig. 18(b), while the two sides are still connected by thin horizontal plates at the top and bottom of the cantilever in case (a). Comparing between cases (b) and (c), the opening that separates the two sides of the section views is much wider in case (c) than in case (b), which corresponds to a smaller material volume fraction. The two walls in the section views of case (c) are thinner than in case (b); there is hardly any bulk material in them.

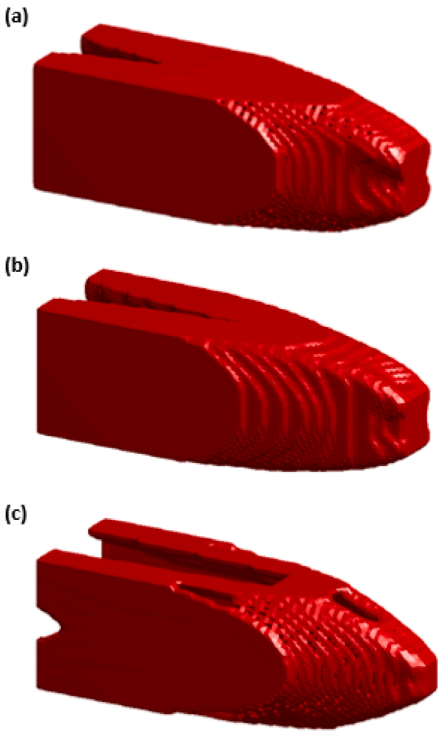

Prescribed volume fraction limit	$\bar{v} = 0.4$
Filter radii	$R_1 = 0.15, R_2 = 0.04.$
Objective value	$f = 814.3$
Material volumes	$V_c = 0.198, V_b = 0.202.$

Prescribed volume fraction limit	$\bar{v} = 0.4$
Filter radii	$R_1 = 0.15, R_2 = 0.08.$
Objective value	$f = 724.8$
Material volumes	$V_c = 0.304, V_b = 0.096$

Prescribed volume fraction limit	$\bar{v} = 0.2$
Filter radii	$R_1 = 0.15, R_2 = 0.08.$
Objective value	$f = 1179.5$
Material volumes	$V_c = 0.177, V_b = 0.023$

Fig. 18. Three 3D cantilever beam results.The selected results on the right are the optimal objective value $\boldsymbol{f}$ (compliance) and the volume fractions of the coating and the bulk materials (denoted by $\boldsymbol{V_c}$ and $\boldsymbol{V_b}$ respectively) in the final topology (color online).

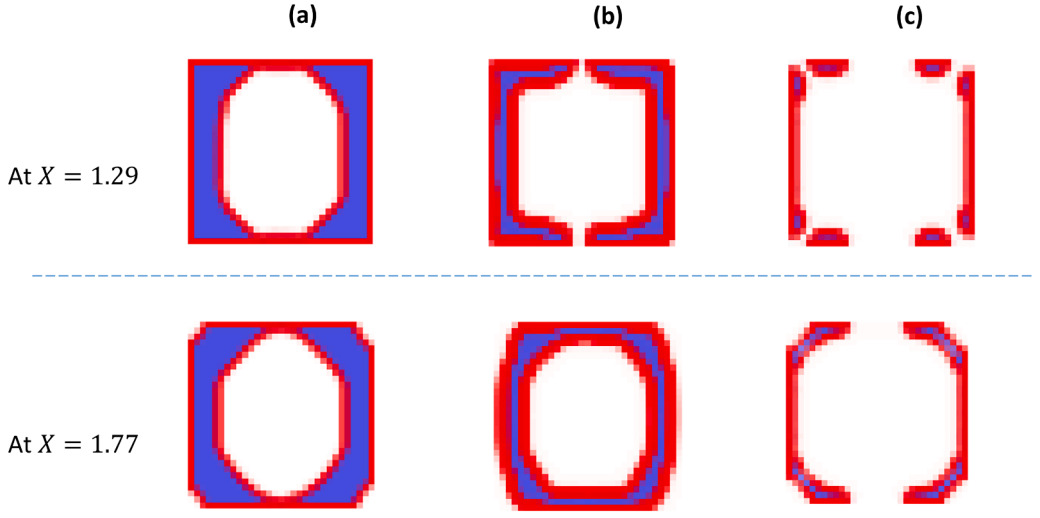

Fig. 19. YZ cross-sectional views of the three results presented in Fig. 18(a), (b), (c) at two X locations: at $\boldsymbol{X} = 1.29$ and $\boldsymbol{X} = 1.77$ (color online).

5. Experimental validation

We want to demonstrate via mechanical testing, that the coated structure design method presented in this work generates improved designs when fabricated by AM than another topology optimization method in which neither material anisotropy (e.g., at infill regions) nor material heterogeneity (e.g., at local surface regions) is considered. The reasoning behind this hypothesis is that this method integrates some AM process-induced material characteristics such as AM process-specific material anisotropy and local material heterogeneity, thus increases the level of correlation between numerical and manufactured designs for a given set of AM process conditions.

The highest correlation between numerical and fabricated designs would be obtained from a topology optimization method in

which all the real-life AM process conditions (local temperature history, hatch patterns, etc.) are considered and modeled precisely. A design resulting from such a method should give the lowest objective value (compliance) than any other design. Let us denote this ideal design by topology 'I'.

Per the above hypothesis, our control case is obtained using an optimization method in which isotropic properties of the raw material (for example, feedstock filament, metal powder) are used on all material regions. In other words, neither material anisotropy nor heterogeneity is considered. This control case is denoted topology 'C'.

In contrast, topology 'E' denotes the solution obtained using the coated structure design method presented in this work, in which material anisotropy produced by an actual AM process as well as local heterogeneity are considered. We will use our method, as demonstrated in the numerical examples, to capture the skin/core structure of FFF tool paths, where the perimeter tool paths correspond to the coating region, and the infill (or core) corresponds to the bulk region. This approach not only models the as-built material numerically but also aligns with the experimental fabrication process, as mentioned in Section 2.2 and explained in more detail in Section 3.3. We will then demonstrate using FFF that a manufactured topology 'E' has improved mechanical performance (i.e., has a higher stiffness) than a manufactured topology 'C' for a given set of AM process parameters. Notice, however, that topology 'E' would not be as good as the ideal design 'I', for there are other real-life AM process conditions that are not accounted for in this coated structure method, such as printing temperature variations and residual stress induced by high temperature.

The reason that we used FFF process instead of PBF processes is that we have easier access to FFF machines, and it is easier to control the printing parameters of the FFF process. To prove the hypothesis, two designs 'E' and 'C' were generated using the 2D MBB beam problem shown in Fig. 4 and then built simultaneously using the same Ultimaker 3 machine and the same PLA filament with the same pre-defined set of process parameters. The 2D MBB beam results were extruded to a depth that is 1/5 of the width H to obtain the designs 'E' and 'C'. Parts were built in the horizontal orientation, that is, the XY coordinate system of the beam shown in Fig. 4 corresponds to the build platform of the Ultimaker machine.

The predetermined printing parameters include an infill pattern of horizontal linear raster lines, and an infill density of 50%. The bulk material of FFF-printed specimens is assumed to exhibit 2D orthotropic properties [6,9,19]. Properties of the bulk material used to compute topology 'E' will be estimated following the above assumptions: Experimentally measured elastic constants of a horizontal infill of 100% density are roughly $E_x = 3388.57\ MPa,\ E_y = 2799.43\ MPa$ based on [8]. Thus, the directional Young's modulus of the bulk material E_{x_bulk} can be deduced, assuming Young's modulus along the raster orientation changes linearly with the fill density:

$$E_{x\_bulk} = 50\% \times 3388.57 = 1694.285\ MPa.$$

The Young's modulus of the bulk material E_{y_bulk} perpendicular to the raster orientation is roughly estimated by approximating the infill region to be a fibrous composite and calculating the elastic modulus transverse to fibers, as explained in [41] Section 5.4.5:

$$E_{y\_bulk} = \frac{E_r E_m}{V_r E_m + V_m E_r} = \frac{E_r}{V_r + V_m \frac{E_r}{E_m}} = \frac{2799.43}{50\% + 50\% \times 100} = 55.43\ MPa.$$

where E_r is the Young's modulus of the fiber (i.e., the infill) perpendicular to the raster orientation (or along the Y-direction), i.e., $E_r = E_y$, and E_m is the Young's modulus of the matrix or the zone of adhesion in-between the linear raster lines along the Y-direction. V_r and V_m are the volume fractions of fiber and matrix, respectively.

The Poisson's ratio can be found in [4]:

$\nu_{xy} = 0.35$, and $\nu_{yx} = \frac{\nu_{xy} E_{y\_bulk}}{E_{x\_bulk}} = \frac{0.35 \times 55.43}{1694.285} = 0.011$.

The approximation of the shear modulus, based on [42], is as follows:

$$G_{xy} = \frac{\sqrt{E_{x\_bulk} E_{y\_bulk}}}{2\left(1 + \sqrt{\nu_{xy}\nu_{yx}}\right)} = \frac{\sqrt{1694.285 \times 55.43}}{2 \times \left(1 + \sqrt{0.35 \times 0.011}\right)} = 144.275\ MPa.$$

The elasticity matrix of the bulk material is then derived from the elastic constants estimated above, using Hooke's law of orthotropic materials, as referenced in [41]:

$$\boldsymbol{D}_{bulk} = \begin{bmatrix} 1701.102 & 19.479 & 0 \\ 19.479 & 55.653 & 0 \\ 0 & 0 & 144.275 \end{bmatrix}$$

The coating material used to compute topology 'E' is assumed to have the same isotropic properties as the feedstock filament. A rough estimate of the feedstock filament properties can be obtained by assuming that the Young's modulus E_x of a horizontal infill of 100% density could attain 90% of that of the feedstock filament (which is assumed to have the same properties as the coating material, $E_{coating}$): $E_{coating} = \frac{E_x}{90\%} = \frac{3388.57}{0.9} = 3765.08\ MPa$. This assumption is supported by the experimental data obtained in [6], in which authors measured and compared the Young's moduli of PLA feedstock wire and tensile specimens with a 0° raster angle where the linear raster patterns are parallel to the load direction.

Considering a Poisson's ratio of $\nu = 0.35$, the elasticity matrix of the coating material can be formed using the two estimated elastic constants and assuming plane stress:

$$\boldsymbol{D}_{coating} = \begin{bmatrix} 4290.69 & 1501.74 & 0 \\ 1501.74 & 4290.69 & 0 \\ 0 & 0 & 1394.47 \end{bmatrix}$$

An optimized topology 'E' obtained using the material properties such as plotted in Fig. 20 is provided in Fig. 21(a1), and a resulting FFF-printed specimen in Fig. 21(a2). The filter radii are $R_1 = 0.15,\ R_2 = 0.03$ for the optimization. The prescribed volume fraction limit is $\bar{v} = 0.4$. The relative mass density (refer to Eq. (2)) is $\lambda_m = 0.5$ to match the pre-defined infill density. Recall from Section 4 that the colors red and blue indicate the coating and the bulk materials respectively, and that only the right half of the MBB beam domain is included in the optimization.

Our control case, topology 'C', is generated using the standard topology optimization framework introduced in [33], in which isotropic material is employed for the entire design domain, i.e., neither material anisotropy nor heterogeneity is considered. The filter radius is set to $R = 0.12$; other input parameters are the same as those used to generate topology 'E', such as the mesh, the volume fraction limit, the SIMP penalty parameter, etc. A design 'C' is provided in Fig. 21(b1), it is a homogeneous structure made of an elastic isotropic material. The fabricated specimen is shown in Fig. 21(b2).

Without experimental testing, we know via visual inspection that the fabricated specimen corresponding to the topology 'E' will demonstrate greater stiffness than the fabricated topology 'C' when tested. For example, the fabricated specimen of topology 'E' (in Fig. 21(a2)) will likely exhibit lower deflection during a three-point bending test, since it is noticeably bulkier than the fabricated specimen 'C' in Fig. 21(b2). Though the two designs have the same prescribed volume fraction limit in the optimization, the infill in the numerical result of topology 'E' is not completely solid, which allows the result to occupy more area. In contrast, the control case assumes solid density throughout the numerical design, which disagrees with the pre-defined deposition strategy.

To produce a design that is more comparable to topology 'E', we use the coated structure design method presented in this work to generate a modified control case 'C_{mod}', but this time, both the coating and the bulk materials are isotropic. In such a design, the difference in material density between the perimeter and the infill region is considered, while material anisotropy is not accounted for. An optimized topology 'C_{mod}' is provided in Fig. 21(c1), its fabricated specimen in Fig. 21(c2). The relative mass density and the relative stiffness between the two materials (refer to Eqs. (2) and (3)) are $\lambda_m = 0.5, \lambda_E = 1$. All other optimization parameters remain unchanged from topology 'E'.

Next, we will demonstrate experimentally that a manufactured topology 'E', such as shown in Fig. 21(a2), has improved mechanical performance (i.e., has a higher stiffness) than a manufactured topology 'C_{mod}', such as shown in Fig. 21(c2), for the pre-determined AM process parameters.

Five sets of specimens were fabricated using the pre-defined deposition strategy and then subjected to three-point bending tests. Each set contains two specimens: one fabricated following topology 'E' and the other following topology 'C_{mod}'. One of the five sets of specimens were provided in Fig. 21(a2) and (c2), which correspond to the topologies 'E' and 'C_{mod}', respectively. The equipment we used to conduct bending tests is shown in Fig. 22. The bending test is carried out under displacement control. The force-displacement curves obtained from one set of ('E', 'C_{mod}') specimens are provided in Fig. 23. Both force and displacement values were negative in the original test data. Their absolute values are used to present the force-displacement curves in Fig. 23. The original force-displacement data, in pounds and inches, were converted to the metric system (in newtons and millimeters), as shown in Fig. 23.

We are only interested in the elastic region of the test data, for linear elasticity is assumed in the coated structure method. To validate the hypothesis, we compare the slopes of the elastic region of the data curves obtained from the two topologies 'E' and 'C_{mod}'. The slope of the force-displacement curve in the elastic region represents the structural stiffness, describing the relationship between the applied force and the resulting displacement. The slopes (or stiffness) are calculated in N/mm.

To calculate the slopes, we selected the same initial portion of the force-displacement curve for both topologies (topology 'E' and topology 'C_{mod}') within each of the five sets of specimens. For the specific set shown in Fig. 23, we selected the initial portion from displacement = 0 to displacement = 1.37 mm for both curves. This selected range represents the early loading phase, where the behavior of each structure remains largely linear based on visual inspection. We then performed linear regression on the selected

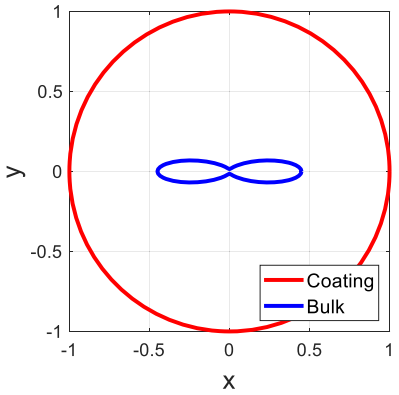

Fig. 20. Contour plots of the tensile moduli of the normalized coating and bulk materials used to obtain topology 'E' (color online).

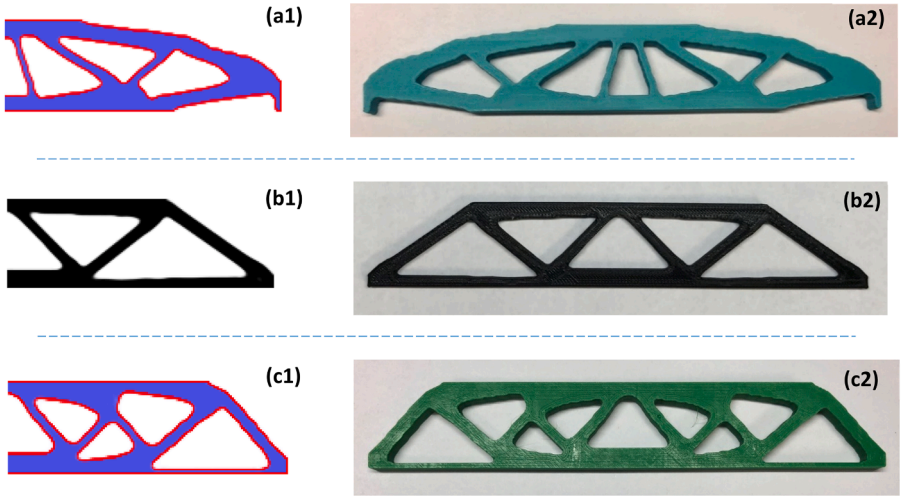

Fig. 21. Results for three different topologies used in experimental validation. (a1), (a2): A numerical result and the corresponding fabricated specimen of topology 'E', respectively. Topology 'E' represents our experimental group that is obtained using the coated structure method and considering material anisotropy produced by an actual AM process as well as local heterogeneity. (b1), (b2): A numerical result and the corresponding fabricated specimen of topology 'C', respectively. Topology 'C' is the original control case in which neither anisotropy nor heterogeneity is considered. (c1), (c2): A numerical result and the corresponding fabricated specimen of topology 'C_{mod}', respectively. Topology 'C_{mod}' is the modified control case that accounts for the difference between the perimeter and the infill region, but does not account for material anisotropy.

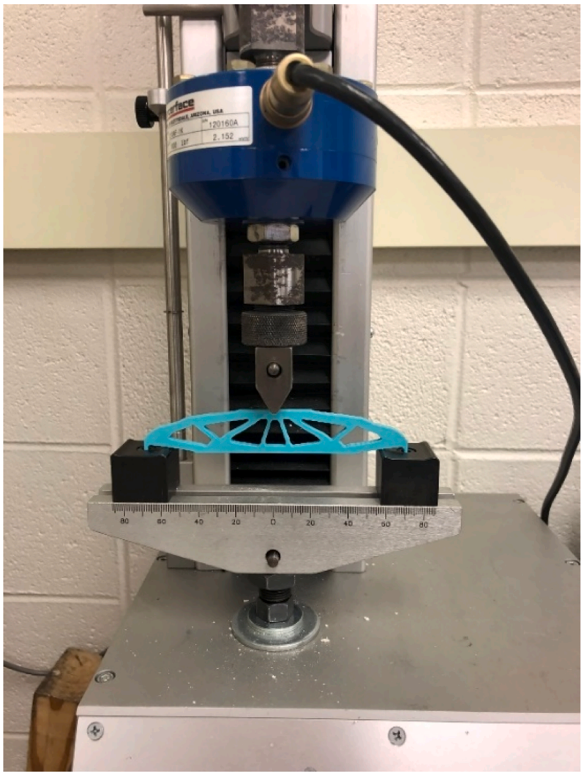

Fig. 22. Photograph of a specimen in the three-point bending test frame. Each end of the specimen is placed on two bearings. A force is applied to the center of the specimen at the top surface using a hydraulic testing machine. The test is carried out under displacement control. The applied force and the displacement of the loading point are measured during the test (color online).

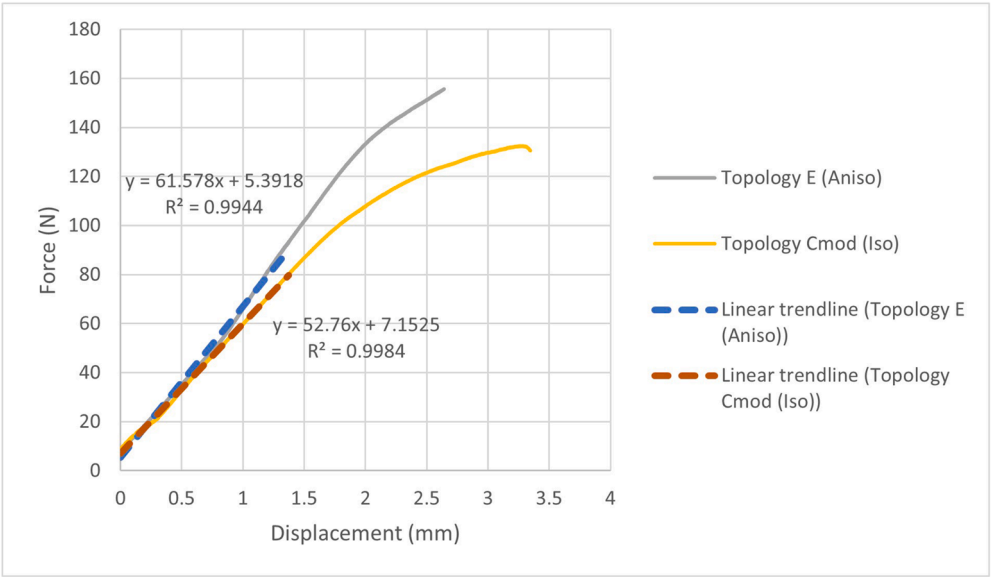

Fig. 23. Force-displacement data obtained from bending tests of one set of ('E', 'C_{mod}') specimens: the solid data curve labeled "Topology E (Aniso)" was obtained by testing the fabricated topology 'E' shown in Fig. 21(a2); the solid curve labeled "Topology Cmod (Iso)" was obtained from the fabricated topology 'C_{mod}' shown in Fig. 21(c2). The dashed line on each solid curve is the linear trendline generated using linear regression applied only to the displacement range from 0 to 1.37 mm of the force-displacement curve. The equation of the best-fit line and the R^2 value are displayed beside each trendline (color online).

portions of the curves to determine the slopes of these mostly linear regions, as shown by the dashed trendlines in Fig. 23, which were only generated for the initial linear portion of the curves, from displacement = 0 to 1.37 mm. The equation of the best-fit line and the R^2 value are displayed next to each trendline, showing that the slopes of the initial linear regions of the force-displacement curves are 61.58 N/mm for topology 'E' and 52.76 N/mm for topology 'C_{mod}' of this particular set of ('E', 'C_{mod}') specimens. The slope (or stiffness) values for the five sets of ('E', 'C_{mod}') specimens are provided in Table 7, where the slopes for the particular set corresponding to Fig. 23 are shaded in blue.

The mean and standard deviation of the stiffness values for the five specimens of each topology (topology 'E' and 'C_{mod}') are calculated and presented in Table 7. For both topologies, the standard deviation is less than 5% of the mean, indicating acceptable consistency between specimens. Furthermore, we observe that the mean slope obtained from topology 'E' is larger than that of topology 'C_{mod}', indicating that topology 'E' has a larger stiffness than the control case 'C_{mod}'. Therefore, we conclude that results obtained using the coated structure method which integrates AM process-induced material anisotropy have improved as-built mechanical performance than results using idealized isotropic properties for a given set of AM process parameters.

6. Concluding remarks

A robust formulation for topology optimization is presented that is developed for a multi-material volume-constrained compliance minimization problem where the materials represent the bulk and coating regions of a part, respectively. The formulation is equipped with material interpolation functions that can identify material-void interfaces of the topology and assign to the interface region a separate material from the interior of the structure. AM process specific material anisotropy and heterogeneity are introduced into the

Table 7
Stiffness values calculated from the slopes of the force-displacement data of five sets of ('E', 'C_{mod}') specimens. The values for the set that corresponds to the data shown in Fig. 23 are highlighted in blue. The mean and standard deviation are provided for each topology.

	Topology 'E' (Aniso) [N/mm]	Topology 'C_{mod}' (Iso) [N/mm]
1	61.14	55.49
2	61.58	52.76
3	56.15	53.31
4	58.30	51.81
5	63.49	54.21
Mean	60.13	53.52
Standard deviation	2.90	1.41

formulation via modification to the material interpolation scheme, to account for the effect of AM processes on material properties. Results with anisotropic candidate materials are provided and compared with those obtained using isotropic materials. Optimized topologies obtained using anisotropic materials vary noticeably from the isotropic case, in such a way that the structure benefits from the directionality of the anisotropic materials. In some 2D cases, for example, material forms truss structures that are aligned with the candidate materials' stiffest tensile direction if the design domain is subjected to bending. The objective value as well as volumes of the coating and bulk materials could change significantly with different anisotropic materials.

Topologically optimized designs obtained using the formulation were 3D-printed and put to mechanical testing. Our numerical method is well connected to the material characteristics illustrated in parts fabricated by additive manufacturing. In additively manufactured parts, local material properties, for example along part boundaries, vary from bulk properties in the rest of the part. In metal printing such as EBM and SLM processes, this is caused by the difference in the microstructure produced by infill hatching and by contour pass respectively. In polymer printing such as FFF process, this is because of the distinction between the infill region and the perimeter shell of an FFF-printed part, which are controlled by different process parameters. The material anisotropy and local heterogeneity present in AM fabricated parts are integrated in the design method. Thanks to this connection, we are able to select a set of AM process parameters that match approximately the parameters used in the numerical method. Via experimental validation, this work demonstrated that the consideration of anisotropic infills is beneficial for the mechanical performance of AM fabricated parts, for it increases the correlation between the topology optimization results and the manufactured designs.

CRediT authorship contribution statement

Yeming Xian: Writing – review & editing, Writing – original draft, Validation, Software, Methodology, Formal analysis, Conceptualization. **Glaucio H. Paulino:** Writing – review & editing, Supervision, Resources, Conceptualization. **David W. Rosen:** Writing – review & editing, Supervision, Resources, Conceptualization.

Declaration of competing interest

The authors declare that they have no known competing financial interests or personal relationships that could have appeared to influence the work reported in this paper.

Acknowledgments

We thank Dr. Emily Sanders for useful suggestions on the formulation and for feedback on the manuscript. We acknowledge funding from NSF projects 2105811 and 2323415.

Replication of results

To facilitate replication of the results, the paper discusses the formulation in detail and provides the essential input parameters for each numerical example.

Data availability

Data will be made available on request.

References

[1] A. Clausen, N. Aage, O. Sigmund, Topology optimization of coated structures and material interface problems, Comput. Methods Appl. Mech. Eng. 290 (2015) 524–541, https://doi.org/10.1016/j.cma.2015.02.011.
[2] J. Wu, A. Clausen, O. Sigmund, Minimum compliance topology optimization of shell–infill composites for additive manufacturing, Comput. Methods Appl. Mech. Eng. 326 (2017) 358–375, https://doi.org/10.1016/j.cma.2017.08.018.
[3] M.P. Bendsoe, Optimal shape design as a material distribution problem, Struct. Optimiz. 1 (4) (1989) 193–202.
[4] J. Torres, J. Cotelo, J. Karl, A.P. Gordon, Mechanical property optimization of FDM PLA in shear with multiple objectives, JOM 67 (5) (2015) 1183–1193, https://doi.org/10.1007/s11837-015-1367-y.
[5] JC Riddick, MA Haile, R Von Wahlde, DP Cole, O Bamiduro, TE. Johnson, Fractographic analysis of tensile failure of acrylonitrile-butadiene-styrene fabricated by fused deposition modeling, Addit. Manuf. 11 (2016) 49–59.
[6] C. Casavola, A. Cazzato, V. Moramarco, C. Pappalettere, Orthotropic mechanical properties of fused deposition modelling parts described by classical laminate theory, Mater. Des. 90 (2016) 453–458.
[7] O.S. Es-Said, J. Foyos, R. Noorani, M. Mendelson, R. Marloth, B.A. Pregger, Effect of layer orientation on mechanical properties of rapid prototyped samples, Mater. Manuf. Process. 15 (1) (2000) 107–122, https://doi.org/10.1080/10426910008912976.
[8] A. Lanzotti, M. Grasso, G. Staiano, M. Martorelli, The impact of process parameters on mechanical properties of parts fabricated in PLA with an open-source 3D printer, Rapid. Prototyp. J. 21 (2015) 604–617.
[9] J. Torres, M. Cole, A. Owji, Z. DeMastry, A.P. Gordon, An approach for mechanical property optimization of fused deposition modeling with polylactic acid via design of experiments, Rapid Prototyp. J. 22 (2) (2016) 387–404.
[10] M. Uddin, M. Sidek, M. Faizal, R. Ghomashchi, A. Pramanik, Evaluating mechanical properties and failure mechanisms of fused deposition modeling acrylonitrile butadiene styrene parts, J. Manuf. Sci. Eng. Trans. ASME 139 (8) (2017) 081018.
[11] S.O. Akande, K. Dalgarno, J. Munguia, Process control testing for fused filament fabrication, Rapid. Prototyp. J. 23 (2017) 246–256.
[12] M.P. Bendsoe, N. Kikuchi, Generating optimal topologies in structural design using a homogenization method, Comput. Methods Appl. Mech. Eng. 71 (1988) 197–224.

[13] E Ulu, E Korkmaz, K Yay, OB Ozdoganlar, LB Kara, Enhancing the structural performance of additively manufactured objects through build orientation optimization, J. Mech. Des. 137 (2015) 111410, https://doi.org/10.1115/1.4030998.
[14] J. Liu, A.T. Gaynor, S. Chen, Z. Kang, K. Suresh, A. Takezawa, L. Li, J. Kato, J. Tang, C.C.L. Wang, L. Cheng, X. Liang, A.C. To, Current and future trends in topology optimization for additive manufacturing, Struct. Multidiscip. Optimiz. 57 (6) (2018) 2457–2483, https://doi.org/10.1007/s00158-018-1994-3.
[15] T. Nomura, E.M. Dede, J. Lee, et al., General topology optimization method with continuous and discrete orientation design using isoparametric projection, Int. J. Numer. Meth. Eng. 101 (2015) 571–605, https://doi.org/10.1002/nme.4799.
[16] P. Zhang, J. Liu, A.C. To, Role of anisotropic properties on topology optimization of additive manufactured load bearing structures, Scr. Mater. 135 (2017) 148–152, https://doi.org/10.1016/j.scriptamat.2016.10.021.
[17] Rosen, D.W., "A set-based design method for material-geometry structures by design space mapping", ASME paper DETC2015-46760.
[18] C. Dapogny, R. Estevez, A. Faure, G. Michailidis, Shape and topology optimization considering anisotropic features induced by additive manufacturing processes, Comput. Methods Appl. Mech. Eng. 344 (2019) 626–665, https://doi.org/10.1016/j.cma.2018.09.036.
[19] J.P. Groen, J. Wu, O. Sigmund, Homogenization-based stiffness optimization and projection of 2D coated structures with orthotropic infill, Comput. Methods Appl. Mech. Eng. 349 (2019) 722–742, https://doi.org/10.1016/j.cma.2019.02.031.
[20] J. Plocher, A. Panesar, Review on design and structural optimisation in additive manufacturing: towards next-generation lightweight structures, Mater. Des. 183 (2019) 108164.
[21] L.E. Murr, E. Martinez, K.N. Amato, S. Gaytan, J. Hernandez, D.A. Ramirez, P.W. Shindo, F. Medina, R.B. Wicker, Fabrication of metal and alloy components by additive manufacturing: examples of 3D materials science, J. Mater. Res. Technol. 1 (1) (2012) 42–54, https://doi.org/10.1016/S2238-7854(12)70009-1.
[22] L E Murr, S M Gaytan, F Medina, E Martinez, J L Martinez, D H Hernandez, B I Machado, D A Ramirez, R B Wicker, Characterization of Ti6Al4V open cellular foams fabricated by additive manufacturing using electron beam melting, Mater. Sci. Eng. A 527 (7–8) (2010) 1861–1868.
[23] S.S. Al-Bermani, M.L. Blackmore, W. Zhang, I. Todd, The origin of microstructural diversity, texture, and mechanical properties in electron beam melted Ti-6Al-4V, Metall. Mater. Trans. A 41 (13) (2010) 3422–3434.
[24] A.A. Antonysamy, J. Meyer, P.B. Prangnell, Effect of build geometry on the β-grain structure and texture in additive manufacture of Ti6Al4V by selective electron beam melting, Mater. Charact. 84 (2013) 153–168.
[25] T.M. Mower, M.J. Long, Mechanical behavior of additive manufactured, powder-bed laser-fused materials, Mater. Sci. Eng. A 651 (2016) 198–213.
[26] K. Kempen, L. Thijs, J. Van Humbeeck, J.-P. Kruth, Mechanical properties of AlSi10Mg produced by selective laser melting, Phys. Proc. 39 (2012) 439–446.
[27] WE Luecke, JA. Slotwinski, Mechanical properties of austenitic stainless steel made by additive manufacturing, J. Res. NIST (2014) 119, https://doi.org/10.6028/jres.119.015.
[28] D. Deng, R.L. Peng, H. Brodin, J. Moverare, Microstructure and mechanical properties of Inconel 718 produced by selective laser melting: Sample orientation dependence and effects of post heat treatments, Mater. Sci. Eng. A 713 (2018) 294–306.
[29] K. Suzuki, N. Kikuchi, A homogenization method for shape and topology optimization, Comput. Methods Appl. Mech. Eng. 93 (1991) 291–381.
[30] N. Olhoff, M.P. Bendsøe, J. Rasmussen, On CAD-integrated structural topology and design optimization, Comput. Methods Applied Mech. Eng. 89 (1991) 259–279.
[31] J. Stegmann, E. Lund, Discrete material optimization of general composite shell structures, Int. J. Numer. Methods Eng. 62 (14) (2005) 2009–2027.
[32] K. Svanberg, Method of moving asymptotes – a new method for structural optimization, Internat. J. Numer. Methods Eng. 24 (2) (1987) 359–373.
[33] C. Talischi, G.H. Paulino, A. Pereira, I.F.M. Menezes, PolyTop: a Matlab implementation of a general topology optimization framework using unstructured polygonal finite element meshes, Struct. Multidiscip. Optim. 45 (3) (2012) 329–357.
[34] BS Lazarov, O Sigmund, Filters in topology optimization based on helmholtz-type differential equations, Int. J. Numer. Methods Eng. 86 (2011) 765–781.
[35] E.D. Sanders, A. Pereira, M.A. Aguiló, G.H. Paulino, PolyMat: an efficient Matlab code for multi-material topology optimization, Struct. Multidiscip. Optim. 58 (6) (2018) 2727–2759.
[36] E.D. Sanders, A. Pereira, G.H. Paulino, Optimal and continuous multilattice embedding, Sci. Adv. 7 (16) (2021) eabf4838.
[37] P.W. Christensen, A. Klarbring, An Introduction to Structural Optimization, Springer, Linköping, 2009.
[38] F. Wang, B. Lazarov, O. Sigmund, On projection methods, convergence and robust formulations in topology optimization, Struct. Multidiscip. Optim. 43 (6) (2011) 767–784, https://doi.org/10.1007/s00158-010-0602-y.
[39] C Talischi, GH Paulino, A Pereira, IFM Menezes, PolyMesher: a general-purpose mesh generator for polygonal elements written in Matlab, Struct. Multidiscip. Optim. 45 (3) (2012) 309–328.
[40] T Zegard, GH Paulino, Bridging topology optimization and additive manufacturing, Struct. Multidisc. Optim. 53 (2016) 175–192, https://doi.org/10.1007/s00158-015-1274-4.
[41] R. Narayanasamy, K. Siva Prasad, N.E. Dowling, Mechanical Behavior of Materials: Engineering Methods For Deformation, Fracture, and Fatigue, Pearson, United Kingdom, 2013.
[42] J. Summerscales, The bulk modulus of carbon fibers, J. Mater. Sci. Lett. 19 (1) (2000) 15–16.
[43] I. Gibson, D. Rosen, B. Stucker, M. Khorasani, Directed Energy Deposition. Additive Manufacturing Technologies, Springer, Cham, 2021, https://doi.org/10.1007/978-3-030-56127-7_10.
[44] M. Zhou, G.I.N. Rozvany, The COC algorithm, Part II: topological, geometrical and generalized shape optimization, Comput. Methods Appl. Mech. Eng. 89 (1–3) (1991) 309–336.
[45] E. Wadbro, B. Niu, Multiscale design for additive manufactured structures with solid coating and periodic infill pattern, Comput. Methods Appl. Mech. Eng. 357 (2019) 112605.
[46] Z. Zhao, X.S. Zhang, Design of graded porous bone-like structures via a multi-material topology optimization approach, Struct. Multidiscip. Optimiz. 64 (2021) 677–698, https://doi.org/10.1007/s00158-021-02870-x.
[47] O. Sigmund, S. Torquato, Design of materials with extreme thermal expansion using a three-phase topology optimization method, J. Mech. Phys. Solids. 45 (6) (1997) 1037–1067.
[48] M.P. Bendsøe, O. Sigmund, Material interpolation schemes in topology optimization, Arch. Appl. Mech. 69 (1999) 635–654.
[49] L.V. Gibiansky, O. Sigmund, Multiphase composites with extremal bulk modulus, J. Mech. Phys. Solids. 48 (3) (2000) 461–498.
[50] M. Stolpe, K. Svanberg, An alternative interpolation scheme for minimum compliance topology optimization, Struct. Multidiscip. Optimiz. 22 (2001) 116–124.
[51] C.F. Hvejsel, E. Lund, Material interpolation schemes for unified topology and multi-material optimization, Struct. Multidiscip. Optimiz. 43 (2011) 811–825.
[52] C.F. Hvejsel, E. Lund, M. Stolpe, Optimization strategies for discrete multi-material stiffness optimization, Struct. Multidiscip. Optimiz. 44 (2011) 149–163.
[53] L. Yin, G.K. Ananthasuresh, Topology optimization of compliant mechanisms with multiple materials using a peak function material interpolation scheme, Struct. Multidiscip. Optimiz. 23 (2001) 49–62.
[54] R. Tavakoli, S.M. Mohseni, Alternating active-phase algorithm for multimaterial topology optimization problems: a 115-line MATLAB implementation, Struct. Multidiscip. Optimiz. 49 (2014) 621–642.
[55] H. Kazemi, A. Vaziri, J.A. Norato, Multi-material topology optimization of lattice structures using geometry projection, Comput. Methods Appl. Mech. Eng. 363 (2020) 112895.
[56] F. Regazzoni, N. Parolini, M. Verani, Topology optimization of multiple anisotropic materials, with application to self-assembling diblock copolymers, Comput. Methods Appl. Mech. Eng. 338 (2018) 562–596.
[57] X. Huang, W. Li, A new multi-material topology optimization algorithm and selection of candidate materials, Comput. Methods Appl. Mech. Eng. 386 (2021) 114114.
[58] X.S. Zhang, G.H. Paulino, A.S. Ramos, Multi-material topology optimization with multiple volume constraints: a general approach applied to ground structures with material nonlinearity, Struct. Multidiscip. Optimiz. 57 (2018) 161–182.
[59] X.S. Zhang, H. Chi, G.H. Paulino, Adaptive multi-material topology optimization with hyperelastic materials under large deformations: A virtual element approach, Comput. Methods Appl. Mech. Eng. 370 (2020) 112976.

[60] M.Y. Wang, X. Wang, Color" level sets: a multi-phase method for structural topology optimization with multiple materials, Comput. Methods Appl. Mech. Eng. 193 (6-8) (2004) 469–496.
[61] M.Y. Wang, S. Chen, X. Wang, Y. Mei, Design of multimaterial compliant mechanisms using level-set methods, J. Mech. Des. 127 (5) (2005) 941–956.
[62] M.Y. Wang, S. Zhou, Synthesis of shape and topology of multi-material structures with a phase-field method, J. Computer-Aided Mater. Des. 11 (2004) 117–138.
[63] S. Zhou, M.Y. Wang, Multimaterial structural topology optimization with a generalized Cahn–Hilliard model of multiphase transition, Struct. Multidiscip. Optimiz. 33 (2007) 89–111.
[64] R. Tavakoli, Multimaterial topology optimization by volume constrained Allen–Cahn system and regularized projected steepest descent method, Comput. Methods Appl. Mech. Eng. 276 (2014) 534–565.
[65] L. Blank, M.H. Farshbaf-Shaker, H. Garcke, C. Rupprecht, V. Styles, Multi-material phase field approach to structural topology optimization, Trends PDE Constrained Optimiz. (2014) 231–246.
[66] X. Huang, Y.M. Xie, Bi-directional evolutionary topology optimization of continuum structures with one or multiple materials, Comput. Mech. 43 (2009) 393–401.